

A NEW APPROACH TO IDENTIFYING THE MOST POWERFUL GRAVITATIONAL LENSING TELESCOPES

KENNETH C. WONG¹, ANN I. ZABLUDOFF¹, S. MARK AMMONS², CHARLES R. KEETON³, DAVID W. HOGG⁴, AND ANTHONY H. GONZALEZ⁵*Draft version April 23, 2013*

ABSTRACT

The best gravitational lenses for detecting distant galaxies are those with the largest mass concentrations and the most advantageous configurations of that mass along the line of sight. Our new method for finding such gravitational telescopes uses optical data to identify projected concentrations of luminous red galaxies (LRGs). LRGs are biased tracers of the underlying mass distribution, so lines of sight with the highest total luminosity in LRGs are likely to contain the largest total mass. We apply this selection technique to the Sloan Digital Sky Survey and identify the 200 fields with the highest total LRG luminosities projected within a $3\frac{1}{2}$ radius over the redshift range $0.1 \leq z \leq 0.7$. The redshift and angular distributions of LRGs in these fields trace the concentrations of non-LRG galaxies. These fields are diverse; 22.5% contain one known galaxy cluster and 56.0% contain multiple known clusters previously identified in the literature. Thus, our results confirm that these LRGs trace massive structures and that our selection technique identifies fields with large total masses. These fields contain 2 – 3 times higher total LRG luminosities than most known strong-lensing clusters and will be among the best gravitational lensing fields for the purpose of detecting the highest redshift galaxies.

Subject headings: galaxies: clusters: general — gravitational lensing: strong

1. INTRODUCTION

Gravitational lensing by galaxy clusters is an important tool for studying the high-redshift universe. Galaxies at redshifts $1 \lesssim z \lesssim 3$ can be magnified into extended arcs, enabling studies of these sources at spatial resolutions beyond what is feasible in similar unlensed objects (e.g., Brammer et al. 2012; Frye et al. 2012; Livermore et al. 2012; Sharon et al. 2012; Yuan et al. 2012). Lensing by foreground galaxy clusters can also magnify very high-redshift ($z \gtrsim 7$) sources into detectability, allowing us to measure their physical properties (e.g., Kneib et al. 2004; Pelló et al. 2004; Schaerer & Pelló 2005; Richard et al. 2006, 2008; Stark et al. 2007; Bradley et al. 2008, 2012; Zheng et al. 2009, 2012; Laporte et al. 2011; Bouwens et al. 2012; Hall et al. 2012; Coe et al. 2013) and making them ideal targets for spectroscopic follow-up (e.g., Bradač et al. 2012). Such studies are particularly important for characterizing objects on the faint end of the galaxy luminosity function at these redshifts, as even the deepest *HST* observations in blank fields require too large a time investment to probe to such depths.

The lensing power of foreground clusters depends on a variety of physical properties. The total mass of the cluster is very important, as the lensing strength depends on the surface mass density of the lens. Wong et al.

(2012) found that distributing the mass among multiple cluster-scale halos along the line of sight (LOS) can increase the lensing cross section compared to having the same mass in a single rich cluster. This effect results from interactions among the multiple lens potentials, boosting the magnification in the field. Analysis of the Millennium (Springel et al. 2005) and Millennium XXL (Angulo et al. 2012) simulations shows that lines of sight with large total masses may contain multiple massive ($\gtrsim 10^{14} M_\odot$) halos and produce some of the highest lensing cross sections in the universe (K. D. French et al. 2013, in preparation). Individual halo properties, including concentration, ellipticity, orientation, and redshift also affect lensing cross sections (e.g., Bartelmann et al. 1995; Meneghetti et al. 2003; Wong et al. 2012).

State-of-the-art lensing analyses focus on fields identified by a single massive cluster (e.g., Postman et al. 2012). Even X-ray surveys (e.g., Böhringer et al. 2000; Vikhlinin et al. 2009) and Sunyaev & Zeldovich (SZ; 1972) effect surveys (e.g., Vanderlinde et al. 2010; Marriage et al. 2011; Williamson et al. 2011) for great lensing fields are biased toward lines of sight with a dominant cluster-scale halo because the signal is not proportional to projected mass. In other words, a line of sight with a single massive cluster looks identical in X-ray or SZ observations to a similar cluster with additional smaller projected halos whose masses may not be sufficient to have a detectable hot X-ray gas component. In X-ray or SZ observations, the scaling of the signal with halo mass is faster than linear (e.g., Bonamente et al. 2008; Vikhlinin et al. 2009), so a line of sight with multiple structures will have a lower signal than if the same total mass were concentrated in a single cluster. Additional lower mass halos, which may not have detectable hot gas components, may be missed entirely in the field. Thus, these studies do not necessarily select for the largest total

¹ Steward Observatory, University of Arizona, 933 North Cherry Avenue, Tucson, AZ 85721

² Lawrence Livermore National Laboratory, 7000 East Avenue, Livermore, CA 94550

³ Department of Physics and Astronomy, Rutgers University, 136 Frelinghuysen Road, Piscataway, NJ 08854

⁴ Center for Cosmology and Particle Physics, Department of Physics, New York University, 4 Washington Place, New York, NY 10003

⁵ Department of Astronomy, University of Florida, Gainesville, FL 32611

mass and/or the most advantageous mass configuration. *The gravitational lenses explored to date may not in fact be the best directions on the sky to look.*

We explore a new optical selection technique to identify the best lines of sight (hereafter referred to as “beams”) for gravitational lensing. By selecting fields that have the greatest total luminosity in luminous red galaxies (LRGs; e.g., Eisenstein et al. 2001), which are biased tracers of the underlying matter distribution (Zehavi et al. 2005; Li et al. 2006; Ho et al. 2009; White et al. 2011) and detectable to high redshifts, we are likely to find beams with the largest single massive halos (galaxy clusters) and with chance alignments of multiple group and cluster-scale halos. This technique requires a wide-field multi-band photometric dataset with accurate redshifts, photometric or spectroscopic. In essence, we are using fewer, but more biased, tracers of the mass along the LOS than methods like the Cluster Red Sequence technique (CRS; Gladders & Yee 2000) and the Gaussian Mixture Brightest Cluster Galaxy algorithm (GMBCG; Hao et al. 2009, 2010) that exploit the relationship between halo mass and red galaxy counts within the halo (Lin et al. 2004). Zitrin et al. (2012) derived mass models of clusters in the Hao et al. (2010) GMBCG sample, including some of the most powerful lenses (Einstein radius $> 30''$). Like X-ray and SZ surveys, these approaches may not be sensitive to multiple projected halos, as smaller structures (i.e., poor clusters) may be hard to identify as galaxy overdensities in color-magnitude space. In contrast, even individual LRGs can be indicative of cluster-scale structures (Ho et al. 2009).

The Sloan Digital Sky Survey (SDSS), with its large sky coverage and photometric LRG selection out to $z \sim 0.7$, is ideal for identifying the best lensing beams using LRGs. Most arc-producing lensing clusters are at intermediate redshift ($0.3 \lesssim z \lesssim 0.8$; Bartelmann et al. 1998; Gladders et al. 2003; Hennawi et al. 2007), although higher-redshift lensing clusters have been found (e.g., Huang et al. 2009; Gonzalez et al. 2012). The SDSS is deep enough to probe a volume-limited sample of very bright LRGs ($M_i - 5\log_{10}(h) \lesssim -22.5$) out to $z \sim 0.7$. The 5-band optical photometry provides LRG selection, luminosities, colors, and photometric redshifts for over 10^6 galaxies (e.g., Padmanabhan et al. 2005, 2007; Ross et al. 2011).

We present our beam selection method and apply it to the SDSS, identifying the 200 beams with the highest LRG luminosity concentrations and therefore likely to contain the largest total masses projected within a radius of $3/5$. The LRG photometric redshift distributions show that many of these beams have multiple structures along the line of sight. Follow-up galaxy spectroscopy in the first fields selected using this method has revealed a diversity of structures, including chance alignments of multiple cluster-scale halos and total masses $\gtrsim 2 \times 10^{15} h^{-1} M_\odot$ (S. M. Ammons et al. 2013, in preparation).

We describe our method of selecting massive beams in § 2. In § 3, we apply it to the SDSS, list the highest-ranked beams and their properties, and discuss applications of this method to future surveys. We summarize our main conclusions in § 4. Throughout this paper, we assume a Λ CDM cosmology with $\Omega_m = 0.274$, $\Omega_\Lambda = 0.726$, and $H_0 = 100 h \text{ km s}^{-1} \text{ Mpc}^{-1}$ with

$h = 0.71$. All magnitudes given are on the AB magnitude system (Oke & Gunn 1983).

2. SELECTION OF MASSIVE BEAMS

Our approach to selecting lines of sight with large total masses is based on using LRGs as indicators of massive halos. LRGs are strongly clustered and are biased tracers of massive structure (e.g., Zehavi et al. 2005; Li et al. 2006; Ho et al. 2009; White et al. 2011). They are among the most luminous galaxies in optical light ($L \gtrsim L^*$; Ho et al. 2009) and thus are visible to large distances. LRGs show little variation in their SEDs (Eisenstein et al. 2003; Cool et al. 2008), making them easy to identify through their optical colors in broadband imaging data. They have been surveyed over large regions of the sky, making them useful probes of the evolution of large scale structure over a cosmologically interesting volume (e.g. Eisenstein et al. 2001; Padmanabhan et al. 2005). Projected concentrations of LRGs on the sky are therefore indicative of either an extremely rich galaxy cluster or a superposition of multiple group and cluster-scale halos, given that each individual LRG is likely to occupy an overdense region.

Our selection technique makes use of this relationship between LRGs and massive structures, identifying beams that have the highest total LRG luminosity. The stellar mass-to-light (M_*/L) ratios of LRGs are strongly correlated with their rest-frame colors (Bell & de Jong 2001), which, given their homogeneous SEDs, implies that they have similar M_*/L ratios. Indeed, Kauffmann et al. (2003) find that the M_*/L ratio of galaxies flattens at high luminosities with smaller scatter for redder rest-frame optical wavelengths, and that the most luminous galaxies have the highest M_*/L ratios (see also Zaritsky et al. 2006). As a result, the optical/near-IR luminosities of LRGs can be used to estimate their stellar masses.

Relating the LRG luminosity to the mass of its host halo is complicated by the relatively flat slope and substantial scatter of the stellar-to-halo mass (SHM) relation for halo masses above $\sim 10^{12} M_\odot$ (e.g., Mandelbaum et al. 2006; Yang et al. 2008; Conroy & Wechsler 2009; More et al. 2009; Behroozi et al. 2010, 2012; Moster et al. 2010; Leauthaud et al. 2012). While this scatter is smaller than for the luminosity to halo mass relation (e.g., Yang et al. 2008; Cacciato et al. 2009), stellar mass is still not a precise tracer of halo mass for individual massive galaxies above this threshold. There is a scaling between the mass and luminosity of a galaxy cluster (e.g., Lin et al. 2003, 2006; Tinker et al. 2005; Cacciato et al. 2013a,b), although central galaxies contribute fractionally less to the stellar mass for larger halo masses (Lin & Mohr 2004; Gonzalez et al. 2007; Leauthaud et al. 2012; Lidman et al. 2012), further suggesting that individual LRGs may not give a good estimate of halo mass. On the other hand, this effect should be mitigated when estimating the total mass in a particular field by integrating over all LRGs in the field and in redshift space. Furthermore, many of these galaxies are satellite galaxies of higher mass clusters, which increases the total LRG luminosity in the most massive halos (White et al. 2011; Behroozi et al. 2012). Therefore, lines of sight containing high total

LRG luminosities are likely to have large total masses, either distributed in multiple, projected cluster halos or dominated by a single massive cluster. The former configurations are more challenging to identify through other selection methods.

Simple number counts of LRGs also can be useful, as there is a relationship between number of LRGs and halo mass. However, the relation has large scatter for individual clusters (0.21 dex for $M \sim 10^{15} M_\odot$ clusters; Ho et al. 2009). Using total luminosity is likely to be a better tracer of total mass due to the SHM relation, despite its shallow slope at high masses. In addition, the small number of LRGs in clusters leads to large Poisson errors, whereas we are unlikely to miss the brightest galaxies that contribute the most to the total luminosity. We perform a simple test that demonstrates that using total LRG luminosity provides a better contrast to the field galaxy population than simple number counts (see Appendix A). For completeness, we list there the additional beams that would have been selected using number counts instead.

3. RESULTS & DISCUSSION

In this section, we apply our massive beam selection technique to the SDSS. The SDSS is currently the survey that has the best characteristics for our selection technique. The latest data release includes imaging of roughly a third of the sky in five optical broadband filters. The depth of the photometric observations is sufficient to detect and classify LRGs within $0.1 \leq z \leq 0.7$ (Padmanabhan et al. 2005), where we expect a large number of lensing clusters to lie. The SDSS also includes spectroscopic redshifts for roughly a third of the LRGs. We examine the LRG redshift distributions in a comparison sample of known lensing clusters, comparing these fields to the 200 best beams in the SDSS as ranked by their integrated LRG luminosity. Our top beams have higher total LRG luminosity and potentially more mass than even these known lensing clusters. Roughly 75% of our beams contain known galaxy clusters, confirming the power of our selection technique. We also discuss possible applications of this technique to current and future surveys.

3.1. Defining the LRG Sample

We select our sample of LRGs from the SDSS Data Release 9 (DR9; Ahn et al. 2012). We identify LRGs using a modified version of the photometric selection criteria of Padmanabhan et al. (2005, 2007). The criteria consist of two separate cuts, denoted “Cut I” and “Cut II”, which are designed to select LRGs at $z \lesssim 0.4$ and $z \gtrsim 0.4$, respectively. The details of the LRG selection are given in Appendix B.

The photometric redshifts in the DR9 catalog are computed using the method in Csabai et al. (2003). We limit our sample to LRGs at redshifts $0.1 \leq z \leq 0.7$. At $z \lesssim 0.1$, the Cut I criteria are too permissive, resulting in a large fraction of interlopers and causing biases in the photometric redshifts when compared to spectroscopic redshifts. At $z \gtrsim 0.7$, most objects are at the faint edge of our sample, resulting in larger photometric errors. We do not have enough spectroscopically observed objects to assess the quality of the photometric redshifts beyond this point.

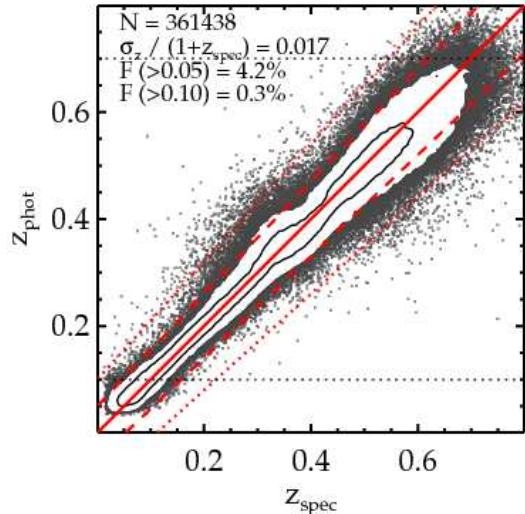


FIG. 1.— Comparison of SDSS DR9 photometric redshifts with SDSS DR9 spectroscopic redshifts. The contours enclose 68% and 95%, respectively, of the galaxies that appear in both samples, with the remaining objects plotted individually (grey points). The red lines represent the 1-to-1 line (solid) and the 5% (dashed) and 10% (dotted) deviations in $\Delta z/(1+z)$. We plot all galaxies, but only calculate statistics for objects with $0.1 \leq z_{\text{phot}} \leq 0.7$, represented by the black dotted lines. We expect the most powerful lenses to lie within this redshift range. We exclude objects at redshifts $z \leq 0.1$ due to biases in the photometric redshifts and the unfavorable lensing geometry. We exclude objects at $z \geq 0.7$ due to large photometric errors and a lack of spectroscopically observed objects to assess directly the quality of the photometric redshifts. The number of objects, redshift accuracy, and fraction of outliers greater than 5% and 10% in $|\Delta z|/(1+z)$ are given in the top left corner. We find good agreement with the spectroscopic redshifts between $0.1 \leq z_{\text{phot}} \leq 0.7$, suggesting that our chosen redshift range is reasonable.

We find good agreement of the photometric redshifts with the DR9 spectroscopic redshifts between $0.1 \leq z \leq 0.7$ (Figure 1). We define the photometric redshift accuracy to be the normalized median absolute deviation, $\sigma_z/(1+z) \equiv 1.48 \times \text{median}(|\Delta z|/(1+z))$. For objects with $0.1 \leq z_{\text{phot}} \leq 0.7$, we calculate $\sigma_z/(1+z) = 0.017$, with catastrophic outlier rates of 4.2% with $|\Delta z|/(1+z) > 0.05$ and 0.3% with $|\Delta z|/(1+z) > 0.1$. The photometric redshifts are unbiased to within $|\overline{\Delta z}|/(1+z) \leq 0.01$ for most of the redshift range probed. There is a slight bias at the $|\overline{\Delta z}|/(1+z) \leq 0.02$ level at $0.6 \leq z \leq 0.7$, which affects less than 10% of our sample. The subsample of objects at the faint end of our magnitude range show the same behavior as the full sample and do not contain additional biases.

To improve the redshift accuracy of our sample, we replace the LRG photometric redshifts and errors with SDSS spectroscopic redshifts and errors where available, which is roughly for one-third of the LRG sample. The redshift uncertainties and outlier rates given in Figure 1 are thus upper limits. Hereafter, when referring to an LRG’s redshift and its uncertainty, we mean the spectroscopic redshift when available and the photometric redshift otherwise.

In deriving the LRG luminosities, we account for K-corrections and luminosity evolution using an elliptical galaxy template generated by evolving a Bruzual & Charlot (2003) stellar population synthesis

model. De Lucia et al. (2006) find that massive elliptical galaxies in dense environments have roughly solar metallicities and stellar populations with a median formation redshift of $z \sim 2.5$ for $M_* \gtrsim 10^{11} M_\odot$, with higher formation redshifts for more massive systems. Similar formation redshifts for massive ellipticals are supported by observational studies (e.g., van Dokkum & Stanford 2003; Treu et al. 2005a,b; Pérez-González et al. 2008). There is evidence that massive early-type galaxies are well-characterized by a Salpeter (1955) initial mass function (e.g., Auger et al. 2010; Treu et al. 2010) or even more bottom-heavy IMFs (e.g., Cappellari et al. 2012; Conroy & van Dokkum 2012; Spiniello et al. 2012; van Dokkum & Conroy 2012). Therefore, we generate the template SED assuming an instantaneous burst of star formation at $z = 3$ with a Salpeter IMF and solar metallicity.

We perform K-corrections using the template SED at the age of the galaxy at its observed redshift, and the model is then passively evolved to $z = 0$. All galaxy luminosities are normalized to $z = 0$ quantities to ensure a fair comparison of their luminosities. We use a single model instead of fitting templates to the observed photometry (e.g., Eisenstein et al. 2001), as LRGs are typically red, quiescent galaxies with little recent star formation and very homogeneous SEDs (Eisenstein et al. 2003; Cool et al. 2008). Furthermore, we are interested in corrections to the rest-frame i -band, which for the template fitting method can only be determined beyond $z \sim 0.2$ by extrapolating the fits to redder rest-frame wavelengths than are covered by the SDSS photometry. We choose the i -band because it is less affected by extinction and tends to trace stellar mass, and thus total mass, better than bluer filters as a result of being less sensitive to recent star formation.

We also only include objects with derived absolute magnitudes within the broad range $-24.7 < M_i - 5\log_{10}(h) < -21$ to eliminate objects with spurious photometric redshifts or aberrant inferred luminosities, while retaining the most luminous LRGs. We visually inspect objects at the bright end of this range to ensure that we include the brightest LRGs in our sample. Our final sample contains 1,151,117 LRGs, of which 361,438 have spectroscopic redshifts.

3.2. Characteristics of the LRG Sample

Here, we investigate the properties of our final SDSS LRG sample. The redshift and i -band luminosity (after accounting for K-corrections and luminosity evolution) distributions of our sample are shown in Figure 2.

In the left panel of Figure 2, the spike in the LRG redshift histogram at $z \sim 0.35$ and trough at $z \sim 0.4$ arise from the combination of several effects. $z \sim 0.35$ is roughly the redshift at which the 4304 Å G-band absorption feature is redshifted into the SDSS r -band, which can masquerade as the 4000 Å break in color-redshift space. As a result, the photometric selection criteria select an excess of galaxies around this redshift. This bias also affects our spectroscopic subsample and in spectroscopic LRG samples with similar photometric selection criteria (e.g., Zehavi et al. 2005). Secondly, the transition between galaxies selected by the Cut I and Cut II criteria is roughly at $z \sim 0.4$. Cut I has an apparent magnitude cut at $r < 19.7$, whereas Cut II has a cut at

$i < 20$. This results in a sharp decrease in the number of Cut I-selected LRGs around $z \sim 0.4$ because we hit the $r < 19.7$ magnitude limit. Meanwhile, Cut II, while probing fainter objects, is optimized to select LRGs at $z \sim 0.5$ and is less efficient at $z \sim 0.4$. This results in a deficit of LRGs around $z \sim 0.4$, accentuating the $z \sim 0.35$ peak.

In addition to these selection effects, there is a small photometric redshift bias in the range $0.3 \lesssim z \lesssim 0.4$ at the $|\Delta z|/(1+z) < 0.01$ level that pulls galaxies toward $z \sim 0.35$, despite the fact that the photometric redshifts remain unbiased overall. The spectroscopic LRG subsample is not affected by this problem. Around this redshift, LRGs transition nearly orthogonally in color-color space, leading to a degeneracy that makes the photometric redshifts less precise, as was also noted by Padmanabhan et al. (2005). This bias, while still small, conspires with the other effects to “sharpen” the spike at $z \sim 0.35$, which was already present due to the selection effects discussed above. This feature is not in the photometric redshift distribution of the Padmanabhan et al. (2005) LRG sample due to known biases in their photometric redshifts that drive some objects with true redshifts near $z \sim 0.35$ to photometric redshifts of $z \sim 0.4$, smoothing out the feature. For $\sim 62\%$ of the galaxies with photometric redshifts in the range $0.3 \leq z \leq 0.4$ and a measured spectroscopic redshift, the absolute difference between the photometric and spectroscopic redshift is smaller than the photometric redshift error given in the SDSS catalog.

In Figure 3, we plot the distribution of LRG absolute i -band magnitudes as a function of redshift. The redshift axis has been rescaled so that it is linear in the enclosed comoving volume within a survey area of π steradians. The sharp edge at the lower right where LRG selection is truncated represents the apparent magnitude cut at $i < 20$ for the Cut II objects. The sharpness of this cutoff is due to our single-model method of handling K-corrections and luminosity evolution. Applying a template-fitting method to the observed photometry (e.g., Eisenstein et al. 2001) would result in scatter about this cutoff. The “sawtooth” feature at $z \sim 0.4$, which is also in the LRG redshift-luminosity distribution of Padmanabhan et al. (2007), results from the $r < 19.7$ apparent magnitude cut for the Cut I objects and corresponds to the trough in the redshift distribution (see Figure 2). This visualization shows that our LRG selection is approximately volume-limited out to $z = 0.4$ for $M_i - 5\log_{10}(h) \lesssim -21$ and to our upper redshift limit of $z = 0.7$ for $M_i - 5\log_{10}(h) \lesssim -22.5$, with the caveat that our selection is less efficient around $z \sim 0.4$.

3.3. LRG Properties of Known Lensing Cluster Fields

We examine the LRG properties of a sample of known strong lensing clusters from Hennawi et al. (2008) and the Cluster Lensing and Supernova Survey with Hubble (CLASH; Postman et al. 2012) that lie within our chosen redshift range and overlap the sky coverage of our SDSS LRG sample. Our goal is to identify the best lensing fields using our new selection technique, and this set of known lensing clusters provides a calibration to which we can compare the LRG properties of our new beams (§ 3.4). If our beams have more total LRG luminosity (\sim mass) than known strong lenses,

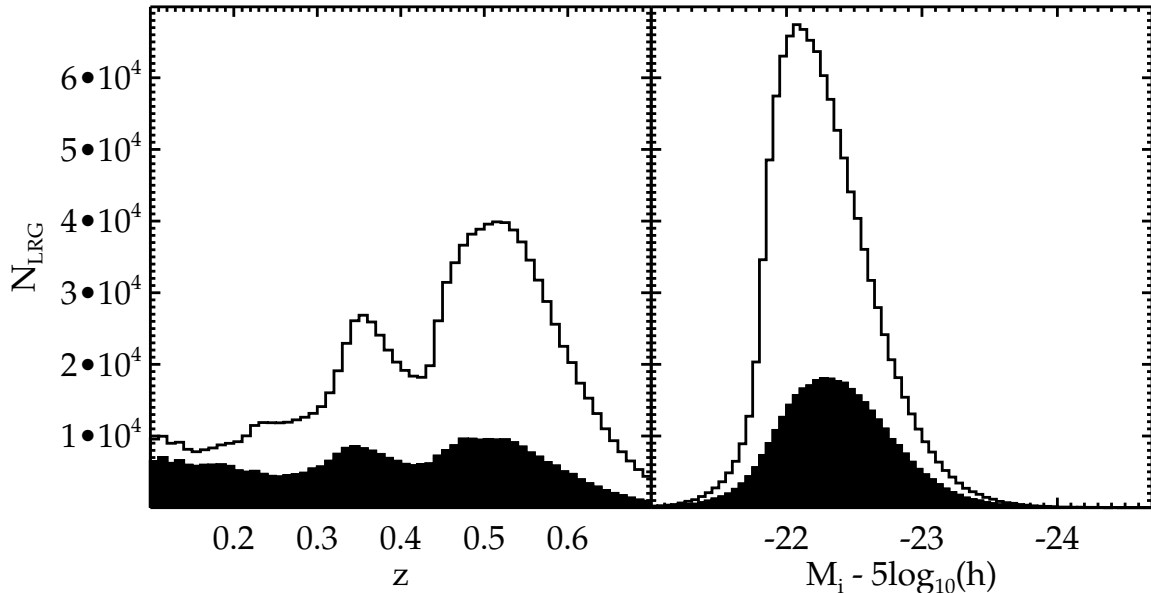


FIG. 2.— Distribution of redshift (left) and i -band absolute magnitude (right) for our LRG sample. The open histogram shows the distribution for all LRGs, while the shaded histogram shows the LRGs with spectroscopic redshifts. The spike in the redshift histogram at $z \sim 0.35$ and trough at $z \sim 0.4$ arise from the combination of several effects, including misidentification of the 4000 \AA break in the photometric selection criteria, the transition between the Cut I and Cut II criteria, and photometric redshift biases.

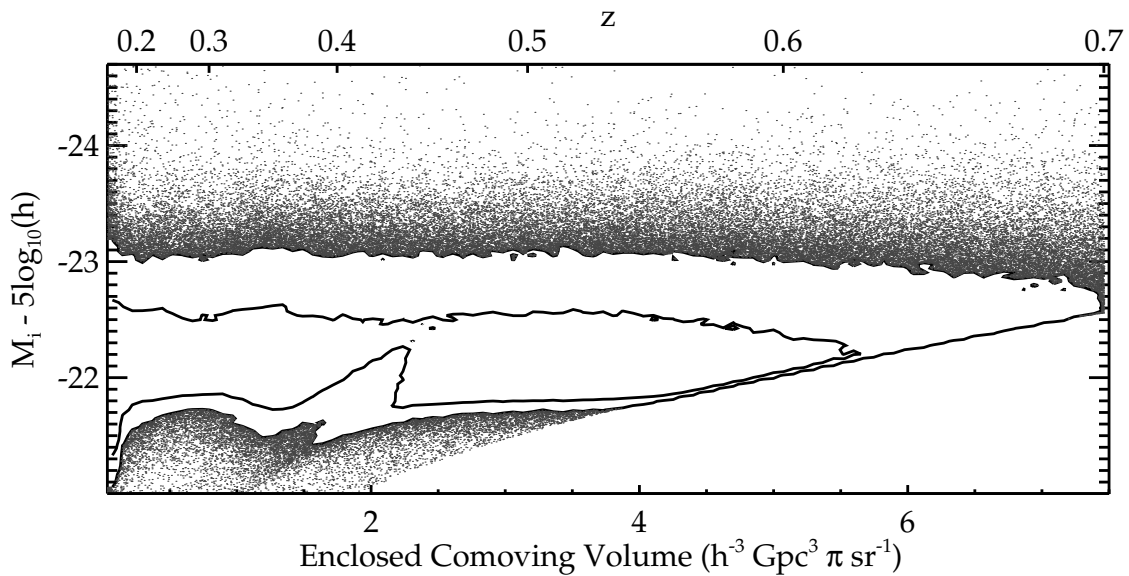


FIG. 3.— Absolute i -band magnitude as a function of comoving volume enclosed within a survey of π steradians at the redshift of each LRG. The contours include 68% and 95% of the LRGs, respectively, with the remaining LRGs plotted individually. The redshift is indicated by the upper x-axis. This visualization shows that our LRG selection is approximately volume-limited out to $z \approx 0.4$ for $M_i - 5\log_{10}(h) \leq -21$ and to our upper redshift limit of $z = 0.7$ for $M_i - 5\log_{10}(h) \lesssim -22.5$, with the caveat that our selection is less efficient around $z \sim 0.4$.

as well as multiple lensing planes in some cases, it is likely that they comprise a better sample of strong lenses. Hennawi et al. (2008) select their sample from the SDSS using the CRS selection method to identify clusters between $0.1 \lesssim z \lesssim 0.6$. We only use those systems labeled by Hennawi et al. (2008) as “definite” or “tentative” lensing clusters from visual identification of lensed arcs. The CLASH sample is a mostly X-ray selected sample of 20 massive clusters with an additional five known lensing clusters. Abell 2261 is in both samples, but we

treat it as a part of the CLASH sample here.

We identify LRGs in these fields within an aperture of $3/5$ (as we do for our SDSS beams in § 3.4) and show their redshift distributions in Figure 4. In many fields, even the massive lensing cluster is marked by only a few LRGs. By selecting beams from SDSS that have a larger total luminosity in LRGs than these fields, we maximize the chance of finding mass concentrations that can act as powerful lenses. While these comparison fields tend to be single mass concentrations, several show non-negligible

mass concentrations projected along the line of sight that are unassociated with the main cluster. Thus, the lens modeling of these known clusters should account for LOS mass concentrations. Such effects have not been explicitly treated in most past analyses, but can influence the inferred mass model (e.g., Hoekstra et al. 2011).

3.4. Selection of SDSS Beams

To find beams with high total LRG luminosity, we search a fixed angular radius around each LRG in our sample. In principle, this selection can be performed with an arbitrary search radius. For our search, we choose an aperture of radius $3\frac{1}{5}$. Chance projections of the most massive clusters ($\sim 10^{15} M_{\odot}$) tend to benefit from interactions among their lens potentials (Wong et al. 2012), even in regions beyond their Einstein radii. In particular, the boost at intermediate magnifications ($\mu \sim 3-10$) due to lensing interactions at larger radii is critical in increasing the detectability of very high-redshift lensed galaxies. Beyond $3\frac{1}{5}$, the strength of these interactions fall off to the point where the halos can be treated as independent lensing fields. Furthermore, typical ground-based near-infrared detectors that are well suited for follow-up observations of lensed high-redshift galaxies have fields of view roughly this size or larger.

For each beam centered on an LRG, we tabulate the total number of LRGs within the aperture, as well as the integrated rest-frame *i*-band luminosity of those LRGs as a proxy for total mass in the beam. We rank all the beams centered on an LRG in descending order by the total LRG luminosity in the beam. Overlapping beams containing the same LRGs but that are centered on different LRGs are further ranked by the luminosity of the LRG at the beam center. This choice makes it more likely that in beams with single dominant clusters, we select the central galaxy, which is often the most luminous (Lin & Mohr 2004), though not always (e.g., von der Linden et al. 2007; Coziol et al. 2009; Skibba et al. 2011; Hikage et al. 2012). Starting from the beam with the highest total luminosity and moving down this ranked list, we construct our list of top beams. If a beam is centered on an LRG that has already been included as part of a previous beam, we skip over that beam, but allow LRGs within it to be counted in beams further down the list. This method makes it possible for an LRG to be part of multiple beams, but minimizes overlap among beams in dense regions. There will always be some beams adjacent to or overlapping one another whose centers are separated by slightly more than the selection radius. While these beams could be counted as a single field for follow-up purposes, we count them as separate beams for consistency. In our final catalog of the top 200 beams, there are 28 that overlap another beam in the top 200.

This method can find beams containing dense concentrations of LRGs (e.g., clusters), but may not necessarily be centered on a cluster center. This can occur if an LRG in the outer parts of a cluster has other LRGs within $3\frac{1}{5}$ of it that are not within $3\frac{1}{5}$ of the more central LRGs of that cluster. This is not a flaw in the methodology as we are not specifically looking for fields centered on a single dense cluster. Rather, our selection is more likely to find lines of sight containing multiple mass concentrations. We do not account for the boundaries of the

survey region when performing our beam selection. This is conservative because we can only underestimate the total luminosity of LRGs in a given field by ignoring these edge effects.

We compare the total luminosity and total number of LRGs in our full sample of beams to that of the comparison sample of lensing clusters from Hennawi et al. (2008) and CLASH in Figure 5. Both the Hennawi et al. (2008) and CLASH samples tend to have lower total LRG luminosity and number counts compared to the SDSS beams, suggesting that our beams at the extreme tail of these distributions contain larger total masses.

We present a list of the 200 best beams as ranked by their total LRG luminosity in Table 1. We choose a sample size of 200 because this is roughly the beam rank above which our beams exceed the total LRG luminosities of massive lensing clusters. These top 200 beams have total LRG luminosities 2–3 times greater than the average total LRG luminosity of the comparison sample. We do recover five of the Hennawi/CLASH clusters in our sample, although our beams may be centered on different coordinates that include more LRGs in the field. We find that $\sim 60\%$ of our selected beams overlap with the top 200 beams selected by LRG number counts. For completeness, we provide a separate list of beams in Appendix A that would have been in the top 200 (or had an equal number of LRGs to beams in our top 200) if we had chosen to sort by LRG number counts instead.

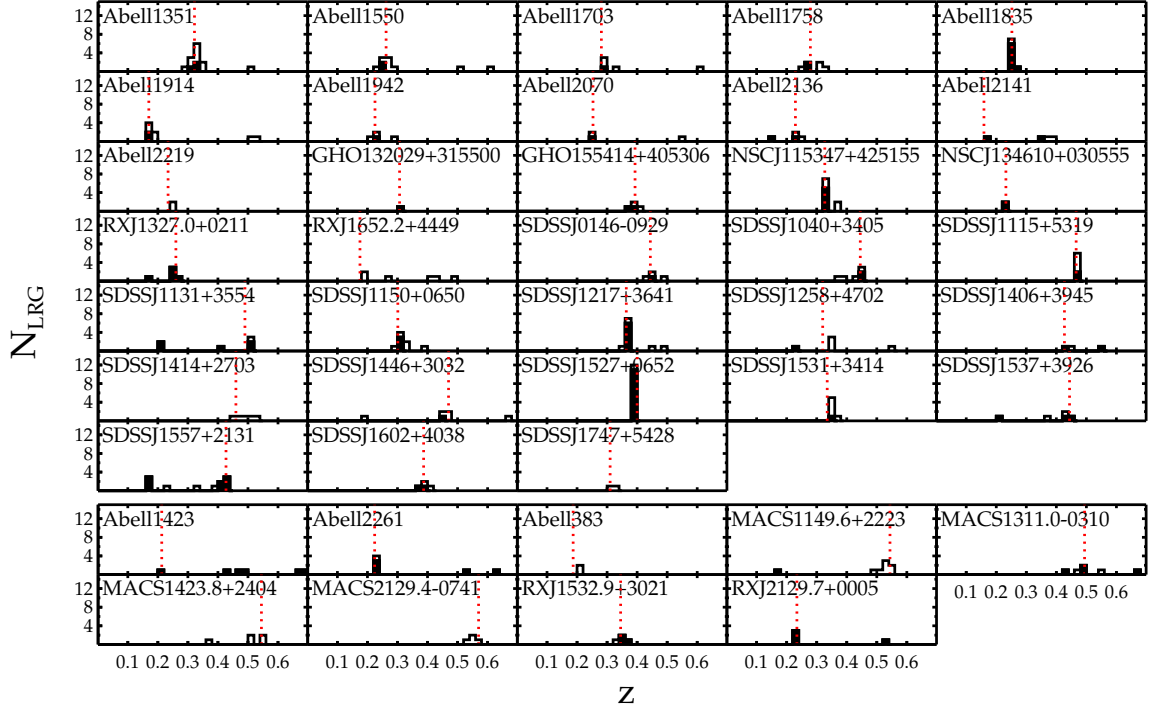


FIG. 4.— Redshift histograms for the LRGs in 33 Hennawi et al. (2008) (top group) and nine CLASH (bottom group) known lensing clusters. The bin size is $\Delta z = 0.02$, roughly the median photometric redshift uncertainty of the LRG sample. The open histograms show the distribution for all LRGs in the beam, while the shaded histograms show those LRGs with spectroscopic redshifts. The redshift of the known cluster is indicated by the dotted red line. Most fields are dominated by a single massive structure, although several have multiple structures distributed throughout redshift space. In most fields, even the massive lensing cluster is marked by only a few LRGs.

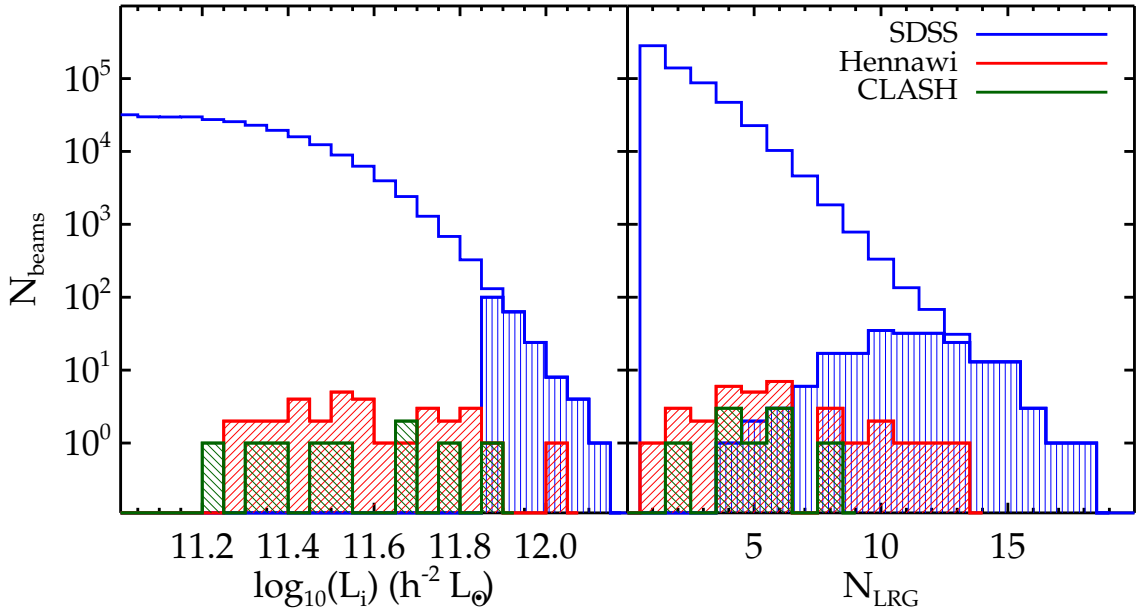


FIG. 5.— *Left*: Histogram of total i -band luminosity of LRGs in each of our SDSS beams (blue). For comparison, we show the same quantity for similar size beams centered on the coordinates of 33 definite and tentative lensing clusters from Hennawi et al. (2008) (red) and nine X-ray and lensing-selected clusters from the CLASH (Postman et al. 2012) survey (green). The shaded blue histogram shows the distribution of total LRG luminosity for our top 200 beams as ranked by total LRG luminosity. *Right*: Histogram of total number of LRGs in each of our selected beams compared to the Hennawi and CLASH beams. The shaded blue histogram represents the LRG number count distribution of the same top 200 beams ranked by total LRG luminosity. Our top 200 beams generally contain larger total LRG luminosity and number counts than even these known lensing clusters. Most of the high-luminosity beams are also the beams with the largest number of LRGs.

TABLE 1
LIST OF SDSS LRG BEAMS

Rank	RA	Dec	N_{LRG}	$\log_{10}(L_i)^a$ ($h^{-2} L_\odot$)	MC $\log_{10}(L_i)^{a,b}$ ($h^{-2} L_\odot$)	MC Rank ^c	Comments ^d	Known Clusters ^e
1	11:23:53.231	+50:52:53.458	15	12.10	$12.08^{+0.02}_{-0.04}$	1	...	3
2	12:44:02.713	+16:51:53.185	16	12.09	$11.99^{+0.05}_{-0.03}$	6	...	4
3	21:28:25.929	+01:33:15.508	13	12.07	$12.06^{+0.03}_{-0.03}$	3	overlaps with 2128+0137	...
4	11:42:24.777	+58:32:05.333	14	12.06	$12.07^{+0.02}_{-0.02}$	2	...	3
5	00:53:29.221	+16:40:29.335	13	12.05	$11.90^{+0.06}_{-0.07}$	52	overlaps with 0053+1637	...
6	23:22:36.940	+09:24:08.046	18	12.04	$11.93^{+0.08}_{-0.08}$	25	overlaps with 2322+0922	...
7	09:49:58.602	+17:08:24.240	14	12.04	$11.99^{+0.03}_{-0.04}$	7	overlaps with 0950+1704	5
8	15:26:13.832	+04:40:30.109	15	12.04	$11.96^{+0.05}_{-0.06}$	17	overlaps with 1526+0439	2
9	10:53:30.330	+56:41:21.327	17	12.02	$11.99^{+0.03}_{-0.03}$	5	...	3
10	02:18:39.886	-00:12:31.752	15	12.02	$11.99^{+0.03}_{-0.05}$	10	...	3
11	10:06:11.170	+08:03:00.487	11	12.01	$11.99^{+0.04}_{-0.04}$	9	...	2
12	11:05:34.246	+17:35:28.209	12	12.00	$11.95^{+0.05}_{-0.06}$	22	overlaps with 1105+1737	2
13	15:10:15.493	+51:45:25.444	13	12.00	$11.97^{+0.04}_{-0.04}$	13
14	16:16:11.888	+06:57:44.695	14	12.00	$11.99^{+0.02}_{-0.02}$	8	overlaps with 1615+0655	5
15	14:17:45.068	+21:18:27.860	12	11.99	$11.98^{+0.03}_{-0.03}$	11	...	3
16	14:01:09.485	-07:50:57.943	14	11.99	$11.97^{+0.04}_{-0.04}$	14
17	02:39:53.126	-01:34:55.980	12	11.99	$12.05^{+0.03}_{-0.03}$	4	...	1
18	08:16:58.695	+49:33:42.953	13	11.99	$11.96^{+0.03}_{-0.03}$	16	...	2
19	01:04:33.196	+12:51:14.258	16	11.99	$11.92^{+0.05}_{-0.06}$	32
20	08:19:53.827	+31:59:57.660	15	11.98	$11.91^{+0.04}_{-0.05}$	37	...	3
21	11:52:08.844	+31:42:35.278	12	11.98	$11.95^{+0.03}_{-0.04}$	20	...	3
22	00:28:32.205	+09:01:02.414	15	11.98	$11.88^{+0.05}_{-0.06}$	71
23	10:50:03.460	+28:29:58.080	12	11.97	$11.98^{+0.03}_{-0.03}$	12	overlaps with 1050+2828	4
24	12:09:15.992	+26:43:33.237	14	11.97	$11.92^{+0.04}_{-0.04}$	33	...	1
25	13:40:46.678	-02:51:50.541	11	11.97	$11.94^{+0.03}_{-0.05}$	24	...	1
26	11:39:26.649	+47:04:27.608	13	11.96	$11.94^{+0.02}_{-0.03}$	23	overlaps with 1139+4704b	3
27	13:51:32.691	+52:03:33.346	14	11.96	$11.85^{+0.07}_{-0.07}$	123	...	2
28	14:37:40.295	+30:12:00.275	12	11.96	$11.95^{+0.03}_{-0.03}$	18	...	3
29	12:43:08.915	+20:22:51.768	14	11.96	$11.88^{+0.05}_{-0.05}$	69	...	3
30	17:43:22.152	+63:42:57.575	11	11.96	$11.90^{+0.05}_{-0.06}$	55	...	3
31	02:02:01.333	-08:29:02.252	12	11.96	$11.89^{+0.07}_{-0.08}$	62	...	4
32	09:10:41.968	+38:50:33.710	13	11.96	$11.91^{+0.03}_{-0.04}$	42	...	3
33	09:42:55.372	+14:27:20.611	13	11.95	$11.95^{+0.03}_{-0.03}$	19	...	2
34	14:33:25.780	+29:27:45.979	15	11.95	$11.93^{+0.02}_{-0.02}$	26	...	4
35	13:06:54.628	+46:30:36.691	11	11.95	$11.95^{+0.03}_{-0.03}$	21	overlaps with 1307+4633	5
36	10:51:34.352	+42:23:29.626	11	11.95	$11.97^{+0.02}_{-0.02}$	15	...	3
37	01:37:26.699	+07:52:09.305	15	11.95	$11.90^{+0.03}_{-0.03}$	54	overlaps with 0137+0755	3
38	17:22:13.049	+32:06:51.773	8	11.95	$11.93^{+0.02}_{-0.03}$	27	...	3
39	12:52:58.597	+23:42:00.034	11	11.95	$11.92^{+0.04}_{-0.04}$	31	...	4
40	01:19:56.788	+12:18:34.735	15	11.95	$11.91^{+0.03}_{-0.04}$	41	...	1
41	00:36:44.118	-21:03:56.989	10	11.95	$11.92^{+0.04}_{-0.05}$	34
42	10:35:35.605	+31:17:47.478	10	11.95	$11.86^{+0.11}_{-0.07}$	92	...	5
43	23:34:23.927	-00:25:00.606	13	11.95	$11.91^{+0.03}_{-0.04}$	36	...	3
44	23:22:53.938	+09:22:51.440	16	11.95	$11.82^{+0.07}_{-0.06}$	155	overlaps with 2322+0924	...
45	15:26:26.690	+04:39:04.707	11	11.95	$11.90^{+0.04}_{-0.05}$	56	overlaps with 1526+0440	1
46	00:01:58.481	+12:03:58.021	7	11.94	$11.72^{+0.04}_{-0.04}$	195	...	2
47	14:39:56.246	+54:51:14.221	15	11.94	$11.86^{+0.05}_{-0.06}$	106	...	3
48	09:43:29.460	+33:18:49.403	13	11.94	$11.91^{+0.03}_{-0.05}$	43	...	5
49	13:22:06.243	+53:53:26.158	10	11.94	$11.91^{+0.05}_{-0.06}$	40
50	22:43:28.058	-00:25:58.808	13	11.94	$11.89^{+0.04}_{-0.03}$	65	...	3

^aTotal rest-frame i -band luminosity in LRGs.

^bMedian of Monte Carlo total luminosity distribution. The error bars represent the difference between the median and the 16/84% quantiles of the distribution.

^cRank when ordered by median of Monte Carlo total luminosity distribution.

^d“Overlap” with another beam means that the beam centers are separated by $< 7'$ and can have LRGs in common.

^eSee Appendix C for details of known clusters in each beam.

TABLE 1
CONTINUED.

Rank	RA	Dec	N_{LRG}	$\log_{10}(L_i)^a$ ($h^{-2} L_\odot$)	MC $\log_{10}(L_i)^{a,b}$ ($h^{-2} L_\odot$)	MC Rank ^c	Comments ^d	Known Clusters ^e
51	15:01:56.456	+33:20:41.059	12	11.94	$11.90^{+0.04}_{-0.05}$	47	...	1
52	02:20:56.845	+06:52:09.157	10	11.94	$11.93^{+0.05}_{-0.05}$	28	...	1
53	01:48:08.231	+00:00:59.692	14	11.93	$11.81^{+0.06}_{-0.07}$	165	...	2
54	09:55:05.022	+28:57:41.137	13	11.93	$11.83^{+0.08}_{-0.08}$	146
55	23:32:19.553	+09:08:21.028	10	11.93	$11.92^{+0.05}_{-0.05}$	35
56	10:39:51.501	+15:27:25.227	10	11.93	$11.90^{+0.04}_{-0.06}$	49	...	3
57	16:15:59.965	+06:55:18.520	15	11.93	$11.91^{+0.03}_{-0.03}$	45	overlaps with 1616+0657	1
58	22:58:30.947	+09:13:49.117	11	11.93	$11.80^{+0.07}_{-0.10}$	167	overlaps with 2258+0915	...
59	01:59:59.711	-08:49:39.704	12	11.93	$11.89^{+0.04}_{-0.05}$	68	...	3
60	10:56:14.771	+28:22:23.064	13	11.93	$11.87^{+0.04}_{-0.06}$	80	...	2
61	09:14:23.778	+21:24:52.512	12	11.93	$11.90^{+0.03}_{-0.03}$	48	...	2
62	09:43:34.462	+03:45:19.979	7	11.93	$11.77^{+0.13}_{-0.21}$	186
63	09:02:16.490	+38:07:07.073	15	11.92	$11.84^{+0.04}_{-0.06}$	127	...	2
64	21:28:19.511	+01:37:42.682	10	11.92	$11.92^{+0.04}_{-0.04}$	30	overlaps with 2128+0133	...
65	16:54:24.482	+44:42:10.793	11	11.92	$11.86^{+0.04}_{-0.04}$	104	...	1
66	09:26:35.472	+29:34:22.128	14	11.92	$11.86^{+0.05}_{-0.05}$	94	...	5
67	15:03:01.311	+27:57:48.781	10	11.92	$11.91^{+0.03}_{-0.04}$	38	...	1
68	00:59:42.039	+13:10:48.304	13	11.92	$11.85^{+0.04}_{-0.05}$	115	overlaps with 0059+1315	...
69	14:33:54.319	+50:40:45.173	11	11.92	$11.87^{+0.04}_{-0.05}$	83	...	2
70	08:53:00.399	+26:22:13.805	11	11.92	$11.88^{+0.03}_{-0.04}$	72	...	2
71	01:25:00.069	-05:31:22.841	15	11.92	$11.89^{+0.04}_{-0.05}$	64
72	11:00:10.270	+19:16:17.104	12	11.92	$11.90^{+0.03}_{-0.04}$	57	...	2
73	23:26:37.180	+11:57:48.578	7	11.92	$11.63^{+0.21}_{-0.12}$	198
74	13:26:36.060	+53:53:57.959	13	11.91	$11.87^{+0.04}_{-0.04}$	76	...	2
75	01:19:34.439	+14:52:08.957	12	11.91	$11.80^{+0.09}_{-0.22}$	169	...	3
76	20:54:38.816	-16:48:57.240	8	11.91	$11.81^{+0.08}_{-0.11}$	164
77	11:56:12.252	-00:21:02.814	11	11.91	$11.90^{+0.03}_{-0.04}$	53	...	2
78	23:17:33.137	+11:51:58.264	12	11.91	$11.80^{+0.07}_{-0.09}$	173
79	12:12:08.759	+27:34:06.919	8	11.91	$11.92^{+0.03}_{-0.03}$	29	...	3
80	16:16:27.616	+58:12:38.798	9	11.91	$11.89^{+0.03}_{-0.03}$	67	...	1
81	12:58:32.002	+43:59:47.314	8	11.91	$11.90^{+0.03}_{-0.04}$	46	...	1
82	08:07:56.920	+65:25:07.350	6	11.91	$11.56^{+0.30}_{-0.07}$	199	...	1
83	10:50:20.408	+28:28:04.966	10	11.91	$11.90^{+0.03}_{-0.03}$	50	overlaps with 1050+2829	2
84	23:19:33.487	-01:19:26.377	10	11.91	$11.90^{+0.04}_{-0.04}$	51	...	2
85	09:21:11.999	+30:29:24.946	14	11.91	$11.86^{+0.04}_{-0.04}$	97	...	2
86	13:04:10.776	+46:37:48.615	8	11.91	$11.85^{+0.04}_{-0.09}$	110
87	12:06:57.409	+30:29:22.828	15	11.91	$11.86^{+0.04}_{-0.05}$	95	...	3
88	15:48:35.149	+17:02:22.535	10	11.91	$11.77^{+0.12}_{-0.12}$	184	...	1
89	09:11:06.757	+61:08:18.085	6	11.91	$11.91^{+0.04}_{-0.05}$	39	...	3
90	02:09:44.322	+27:17:09.282	11	11.91	$11.86^{+0.04}_{-0.05}$	99
91	08:22:49.875	+41:28:12.007	11	11.91	$11.86^{+0.05}_{-0.06}$	103	...	2
92	23:03:44.474	+00:09:38.406	11	11.91	$11.85^{+0.05}_{-0.06}$	124	...	1
93	09:16:14.956	-00:25:31.237	14	11.91	$11.89^{+0.04}_{-0.04}$	63	...	5
94	12:01:25.380	+23:50:58.316	7	11.90	$11.86^{+0.06}_{-0.16}$	93	...	4
95	12:20:34.594	+23:01:06.765	8	11.90	$11.88^{+0.04}_{-0.05}$	70
96	12:42:19.077	+40:23:40.425	10	11.90	$11.87^{+0.03}_{-0.04}$	85	...	2
97	11:59:04.900	+51:11:15.803	13	11.90	$11.85^{+0.03}_{-0.04}$	116	...	1
98	11:11:23.230	+26:01:58.357	12	11.90	$11.90^{+0.03}_{-0.03}$	59	...	3
99	11:23:08.271	+54:01:58.928	10	11.90	$11.67^{+0.05}_{-0.06}$	197	...	1
100	14:32:40.352	+31:41:36.116	7	11.90	$11.76^{+0.15}_{-0.09}$	187	...	2

TABLE 1
CONTINUED.

Rank	RA	Dec	N_{LRG}	$\log_{10}(L_i)^a$ ($h^{-2} L_\odot$)	MC $\log_{10}(L_i)^{a,b}$ ($h^{-2} L_\odot$)	MC Rank ^c	Comments ^d	Known Clusters ^e
101	12:45:04.700	+02:29:08.618	10	11.90	$11.90^{+0.03}_{-0.04}$	58	...	2
102	02:22:47.925	+06:28:11.294	4	11.90	$11.85^{+0.07}_{-0.22}$	113
103	09:15:50.686	+42:57:08.567	13	11.90	$11.84^{+0.03}_{-0.03}$	134	...	2
104	13:41:08.628	+12:33:45.316	9	11.90	$11.81^{+0.07}_{-0.11}$	161	...	1
105	12:25:49.069	+08:24:48.700	11	11.89	$11.88^{+0.03}_{-0.03}$	74	...	1
106	08:31:34.886	+26:52:25.307	13	11.89	$11.86^{+0.04}_{-0.05}$	100	...	3
107	10:14:11.602	+22:31:53.131	12	11.89	$11.73^{+0.03}_{-0.04}$	193	...	3
108	15:36:44.604	+02:46:50.702	12	11.89	$11.87^{+0.04}_{-0.05}$	87	...	2
109	14:54:16.517	+04:34:40.491	8	11.89	$11.86^{+0.04}_{-0.07}$	96	...	1
110	15:27:45.828	+06:52:33.629	12	11.89	$11.89^{+0.03}_{-0.04}$	60	...	3
111	00:06:11.544	-10:28:19.512	13	11.89	$11.87^{+0.05}_{-0.05}$	84	...	4
112	00:46:43.567	-01:52:23.434	13	11.89	$11.81^{+0.05}_{-0.06}$	158
113	00:53:37.578	+16:37:29.457	8	11.89	$11.74^{+0.09}_{-0.08}$	191	overlaps with 0053+1640	...
114	00:15:23.386	-09:18:51.103	12	11.89	$11.86^{+0.05}_{-0.06}$	108	...	2
115	11:16:01.248	+18:24:23.300	9	11.89	$11.91^{+0.04}_{-0.04}$	44	...	1
116	02:04:17.610	-12:34:03.800	10	11.89	$11.83^{+0.05}_{-0.06}$	144
117	00:59:28.085	+13:15:48.171	10	11.89	$11.86^{+0.04}_{-0.04}$	91	overlaps with 0059+1310	...
118	10:42:47.206	+33:12:17.845	11	11.89	$11.73^{+0.07}_{-0.08}$	192	...	1
119	15:33:49.313	+02:38:36.105	11	11.89	$11.81^{+0.05}_{-0.06}$	163	...	2
120	17:52:27.692	+60:10:12.774	10	11.89	$11.83^{+0.05}_{-0.05}$	143	...	1
121	12:08:19.794	+61:22:03.732	10	11.89	$11.84^{+0.05}_{-0.09}$	132	...	1
122	01:19:07.658	-09:34:02.693	13	11.89	$11.82^{+0.05}_{-0.05}$	153	...	2
123	09:38:11.613	+27:35:43.705	8	11.89	$11.89^{+0.03}_{-0.03}$	66	...	3
124	23:02:14.123	+06:49:30.820	11	11.89	$11.80^{+0.05}_{-0.05}$	175
125	14:52:00.837	+01:06:56.447	12	11.88	$11.86^{+0.03}_{-0.05}$	107	...	4
126	12:24:45.458	-00:39:14.796	10	11.88	$11.85^{+0.06}_{-0.06}$	122	...	3
127	15:54:59.348	+51:37:23.214	10	11.88	$11.80^{+0.05}_{-0.07}$	176	...	2
128	22:43:27.197	+20:39:48.807	11	11.88	$11.79^{+0.05}_{-0.05}$	181
129	12:19:21.841	+50:53:28.236	11	11.88	$11.84^{+0.05}_{-0.05}$	139	...	3
130	09:51:40.088	-00:14:20.218	6	11.88	$11.86^{+0.03}_{-0.04}$	90	...	3
131	00:51:24.585	-10:49:09.758	12	11.88	$11.79^{+0.05}_{-0.08}$	179	...	1
132	22:26:27.277	+00:53:29.136	12	11.88	$11.87^{+0.02}_{-0.02}$	86	...	1
133	15:12:31.251	+17:12:15.057	8	11.88	$11.80^{+0.06}_{-0.09}$	166
134	15:50:36.108	+39:48:56.718	9	11.88	$11.84^{+0.04}_{-0.04}$	133	...	3
135	11:33:41.604	+39:52:25.291	9	11.88	$11.85^{+0.03}_{-0.03}$	114	...	5
136	13:01:02.878	+05:35:29.711	10	11.88	$11.84^{+0.04}_{-0.05}$	131	...	2
137	21:55:56.718	+05:49:22.752	12	11.88	$11.84^{+0.03}_{-0.04}$	130
138	11:33:37.447	+66:24:44.842	11	11.88	$11.81^{+0.05}_{-0.06}$	162	...	2
139	01:57:54.644	-00:57:11.347	12	11.88	$11.79^{+0.07}_{-0.10}$	180	...	1
140	11:13:46.352	+56:40:34.462	14	11.88	$11.80^{+0.07}_{-0.07}$	168	...	3
141	14:44:19.496	+16:20:12.303	10	11.88	$11.84^{+0.04}_{-0.05}$	135	...	3
142	01:54:36.729	-19:31:19.437	10	11.88	$11.80^{+0.03}_{-0.04}$	170	~20% outside survey edge	...
143	22:24:24.708	-02:39:33.138	11	11.88	$11.85^{+0.04}_{-0.06}$	118
144	10:27:02.072	+09:16:40.107	8	11.88	$11.79^{+0.05}_{-0.07}$	177	...	1
145	16:48:00.199	+33:40:03.887	11	11.88	$11.83^{+0.03}_{-0.04}$	145	...	2
146	10:22:32.057	+50:07:07.870	8	11.88	$11.87^{+0.03}_{-0.03}$	88	...	2
147	09:26:51.422	+04:58:17.559	12	11.88	$11.88^{+0.04}_{-0.05}$	75	...	6
148	12:17:31.158	+36:41:11.240	11	11.88	$11.85^{+0.03}_{-0.06}$	117	...	3
149	11:53:05.648	+41:45:20.510	9	11.87	$11.82^{+0.04}_{-0.08}$	147	...	2
150	14:33:05.416	+51:03:16.905	12	11.87	$11.75^{+0.07}_{-0.08}$	190	...	1

TABLE 1
CONTINUED.

Rank	RA	Dec	N_{LRG}	$\log_{10}(L_i)^a$ ($h^{-2} L_\odot$)	MC $\log_{10}(L_i)^{a,b}$ ($h^{-2} L_\odot$)	MC Rank ^c	Comments ^d	Known Clusters ^e
151	09:01:04.594	+39:54:49.063	10	11.87	$11.84^{+0.04}_{-0.05}$	136	...	1
152	10:50:38.567	+35:49:12.425	13	11.87	$11.80^{+0.05}_{-0.05}$	174	...	1
153	20:55:07.146	-11:44:38.837	10	11.87	$11.87^{+0.03}_{-0.03}$	78
154	08:50:07.915	+36:04:13.650	12	11.87	$11.87^{+0.02}_{-0.03}$	79	...	3
155	17:24:47.122	+32:02:10.676	10	11.87	$11.83^{+0.03}_{-0.04}$	141
156	08:45:43.999	+30:10:07.090	9	11.87	$11.84^{+0.04}_{-0.05}$	140	...	4
157	14:55:07.993	+38:36:04.879	11	11.87	$11.82^{+0.04}_{-0.05}$	150	...	4
158	02:27:57.609	+03:09:16.489	14	11.87	$11.76^{+0.05}_{-0.06}$	188
159	11:07:19.334	+53:04:17.938	9	11.87	$11.86^{+0.04}_{-0.06}$	98	...	2
160	15:38:02.025	+39:27:39.159	8	11.87	$11.87^{+0.03}_{-0.03}$	82	overlaps with 1538+3922	4
161	01:03:24.248	+00:55:37.011	9	11.87	$11.84^{+0.05}_{-0.05}$	126	...	2
162	10:40:17.611	+54:37:08.607	9	11.87	$11.86^{+0.03}_{-0.04}$	109	...	3
163	12:28:58.786	+53:37:27.671	11	11.87	$11.84^{+0.03}_{-0.04}$	125	...	1
164	15:38:04.005	+39:22:32.253	8	11.87	$11.86^{+0.03}_{-0.03}$	101	overlaps with 1538+3927	1
165	01:39:10.116	+07:03:09.893	8	11.87	$11.82^{+0.05}_{-0.04}$	151
166	09:50:00.059	+17:04:27.060	12	11.87	$11.82^{+0.03}_{-0.03}$	154	overlaps with 0949+1708	4
167	10:29:10.561	+33:22:35.618	5	11.87	$11.40^{+0.30}_{-0.24}$	200
168	12:34:49.804	+23:03:42.109	11	11.87	$11.85^{+0.04}_{-0.05}$	111	...	3
169	01:27:10.589	+23:14:19.797	11	11.87	$11.86^{+0.03}_{-0.03}$	105	...	1
170	13:15:23.033	-02:50:35.192	11	11.87	$11.77^{+0.06}_{-0.07}$	185	...	1
171	11:39:02.869	+47:04:43.290	12	11.87	$11.81^{+0.04}_{-0.05}$	159	overlaps with 1139+4704a	2
172	14:31:48.010	+09:00:15.869	13	11.86	$11.72^{+0.07}_{-0.09}$	194	...	1
173	09:47:14.189	+38:10:22.088	11	11.86	$11.85^{+0.04}_{-0.05}$	112	...	3
174	12:17:05.124	+26:05:18.445	13	11.86	$11.84^{+0.04}_{-0.05}$	129	...	1
175	13:26:25.383	+53:24:58.472	12	11.86	$11.82^{+0.04}_{-0.05}$	156	...	1
176	01:53:42.190	+05:35:44.062	10	11.86	$11.87^{+0.04}_{-0.03}$	77	...	1
177	10:54:40.435	+55:23:56.307	7	11.86	$11.85^{+0.02}_{-0.03}$	119	...	2
178	09:58:25.077	+42:39:44.430	9	11.86	$11.82^{+0.07}_{-0.03}$	152
179	00:36:09.793	+23:37:17.923	9	11.86	$11.75^{+0.05}_{-0.06}$	189
180	23:33:42.330	+24:41:06.662	8	11.86	$11.79^{+0.09}_{-0.10}$	178
181	00:40:36.695	+25:29:12.961	10	11.86	$11.80^{+0.04}_{-0.05}$	171
182	14:37:17.666	+34:18:22.187	12	11.86	$11.85^{+0.04}_{-0.04}$	121	...	5
183	14:15:08.392	-00:29:35.680	10	11.86	$11.82^{+0.03}_{-0.02}$	148	...	3
184	20:53:55.128	-06:34:51.054	8	11.86	$11.81^{+0.04}_{-0.06}$	160	...	1
185	12:35:44.353	+35:32:47.968	12	11.86	$11.83^{+0.05}_{-0.06}$	142	...	1
186	11:52:35.385	+37:15:43.111	9	11.86	$11.86^{+0.00}_{-0.03}$	102	...	2
187	14:45:34.036	+48:00:12.417	10	11.86	$11.84^{+0.04}_{-0.05}$	128	...	2
188	08:40:08.745	+21:56:03.214	10	11.86	$11.85^{+0.04}_{-0.05}$	120	...	1
189	13:48:53.073	+57:23:46.617	11	11.86	$11.82^{+0.04}_{-0.04}$	149	...	3
190	13:07:03.631	+46:33:47.849	9	11.86	$11.87^{+0.03}_{-0.03}$	81	overlaps with 1306+4630	6
191	11:40:40.199	+44:07:40.291	9	11.86	$11.84^{+0.04}_{-0.03}$	137	...	5
192	14:48:20.246	+20:43:31.168	10	11.86	$11.82^{+0.04}_{-0.05}$	157	...	2
193	12:41:56.529	+03:43:59.760	5	11.86	$11.86^{+0.02}_{-0.02}$	89	...	2
194	08:41:23.880	+25:13:05.204	9	11.86	$11.84^{+0.03}_{-0.04}$	138	...	2
195	22:58:17.244	+09:15:12.899	9	11.86	$11.78^{+0.07}_{-0.07}$	182	overlaps with 2258+0913	...
196	00:24:59.715	+08:26:16.778	12	11.86	$11.71^{+0.06}_{-0.06}$	196	...	1
197	15:50:16.987	+34:18:33.901	10	11.86	$11.89^{+0.03}_{-0.03}$	61	...	3
198	01:37:18.176	+07:55:44.482	13	11.86	$11.88^{+0.03}_{-0.04}$	73	overlaps with 0137+0752	1
199	11:05:20.978	+17:37:16.830	10	11.86	$11.78^{+0.05}_{-0.06}$	183	overlaps with 1105+1735	3
200	03:33:12.198	-06:52:24.614	10	11.86	$11.80^{+0.06}_{-0.07}$	172	...	1

The redshift distributions of the LRGs in the top 200 beams are shown in Figure 6. The beams show a wide diversity of configurations, including beams dominated by a single massive peak, as well as beams with multiple structures along the line of sight. The latter configurations indicate chance alignments of galaxy clusters or groups in these fields, which can lead to advantageous lensing configurations for magnifying very high-redshift ($z \gtrsim 7$) galaxies (Wong et al. 2012). Even single LRGs can trace massive lensing clusters (see Figure 4).

We show color images of our top 20 beams in Figure 7 to give a sense of the nature of these fields. The images are taken from the SDSS DR9 SkyServer⁶ and show $7' \times 7'$ fields centered on the coordinates of each beam to roughly match our circular selection aperture. The contours overlaid on the images trace the projected galaxy overdensities as determined from the full catalog of primary SDSS photometric galaxies brighter than $r = 22$. The contours generally trace the LRGs, confirming that the LRGs mark the densest structures in these fields. Like the redshift distributions of these beams, the angular distributions show a large diversity. Some beams are dominated by a single concentration of galaxies, whereas others have multiple clumps projected on the sky.

We perform a search in the NASA/IPAC Extragalactic Database (NED) for galaxy clusters that have been identified by past studies within our selected beams. We find that 22.5% of our beams contain one known cluster, and 56.0% contain multiple clusters, confirming the high mass concentrations projected along these lines of sight. We list the number of known clusters in each beam in Table 1 and present a list of these clusters in Appendix C.

We visually inspect the SDSS SkyServer images of each of our top 200 fields. The majority show large concentrations of spheroidal galaxies indicative of cluster-scale structures. The other beams could be chance alignments of smaller group-scale halos, or could contain a number of misclassified objects masquerading as LRGs. While we have limited the number of misclassifications with our selection cuts (see Appendix B), there are inevitably a small fraction of objects that contaminate our LRG catalog. We will describe the first results from our spectroscopic follow-up survey of several of these beams in S. M. Ammons et al. (2013, in preparation).

3.5. Possible Errors in Beam Selection

We use a Monte Carlo method to calculate the uncertainty on the total LRG luminosity of each of our top beams. We begin by searching the SDSS DR9 for all primary photometric objects classified as galaxies within our beams. Objects fainter than $r = 22$ are removed, as this is roughly where the morphological star/galaxy separation breaks down⁷. We replace the photometric redshift and its associated error with a spectroscopic redshift and error where available.

For each beam, we apply Gaussian errors to the quantities defined in our LRG selection criteria (e.g. apparent magnitude, redshift; see Appendix B) over 1000 Monte Carlo trials. For a given trial, we re-determine which galaxies in the beam satisfy the selection criteria and

compute the total LRG luminosity. The final distribution of 1000 total LRG luminosities for each beam therefore accounts for both the intrinsic errors in the galaxy properties themselves, as well as galaxies falling into or out of the LRG selection cuts. Because the resulting luminosity distributions are non-Gaussian in general, we report median values in Table 1. The error bars associated with these median values correspond to the 16% and 84% quantiles of the distribution for each beam. In Figure 8, we plot the observed total luminosity for each beam, along with the median of the Monte Carlo trials with the associated error range.

In general, the medians of the luminosity distributions generated through the Monte Carlo trials tend to be lower than the observed values. This is expected, because these beams were selected to be the top-ranked beams by total LRG luminosity. Given the scatter in the total luminosity, the selected beams are likely those that are among the best and also happen to scatter upwards in observed total LRG luminosity. Also, while this scatter affects the detailed beam rankings relative to the “true” rankings, Figure 8 shows that even among the top 200, there is a noticeable decrease in the median integrated LRG luminosity when ordered by the observed values, indicating that the observed values reliably rank the beams. One may also suspect that our top beams are biased toward low mass-to-light (M/L) ratios. For the initial beams that we have followed-up spectroscopically (S. M. Ammons et al. 2013, in preparation), we compare their M/L ratios to those of a sample of our comparison lensing clusters (§ 3.3) using virial masses from the literature (Mantz et al. 2010; Zitrin et al. 2011; Coe et al. 2012). We find that our beams have roughly comparable M/L ratios, suggesting that a potential bias in M/L is not a dominant effect.

We show the 20-beam central moving average of the median total LRG luminosities of the Monte Carlo trials in Figure 8. While the values trend downward with beam rank as expected, the steepness of the trend noticeably decreases after the first 20 – 30 beams. To test the robustness of our selected beams, we calculate statistics for a larger sample of the top 1000 beams. When re-ranked by the median total LRG luminosities over 200 trials per beam, $\sim 70 - 75\%$ of the beams within the top N beams, where $N \leq 200$, remain within the top N beams. Only five of the top 200 beams fall out of the top 400 when re-ranked in this manner. Thus, most of the top 200 beams are robust to these measurement uncertainties.

As a result of the flux-limited nature of our sample (see Figure 3), the reported LRG luminosities in our beams are probably biased low given that we are not as sensitive to lower-luminosity LRGs at higher redshifts ($z \gtrsim 0.4$). Furthermore, galaxies at higher redshifts that could otherwise scatter into the LRG selection cuts are likely to have larger magnitude errors due to their faintness, which can exclude them from being classified as LRGs based on the r -band magnitude error cut (see Appendix B). Thus, these biases potentially affect beams with high-redshift structures more than ones with the bulk of LRGs at lower redshift.

3.6. Potential Applications to Other Surveys

Our selection method can be applied not just to current surveys like the SDSS, but also to other ongoing

⁶ <http://skyserver.sdss3.org/dr9/>

⁷ See www.sdss3.org/dr9/imaging/other_info.php#stargalaxy

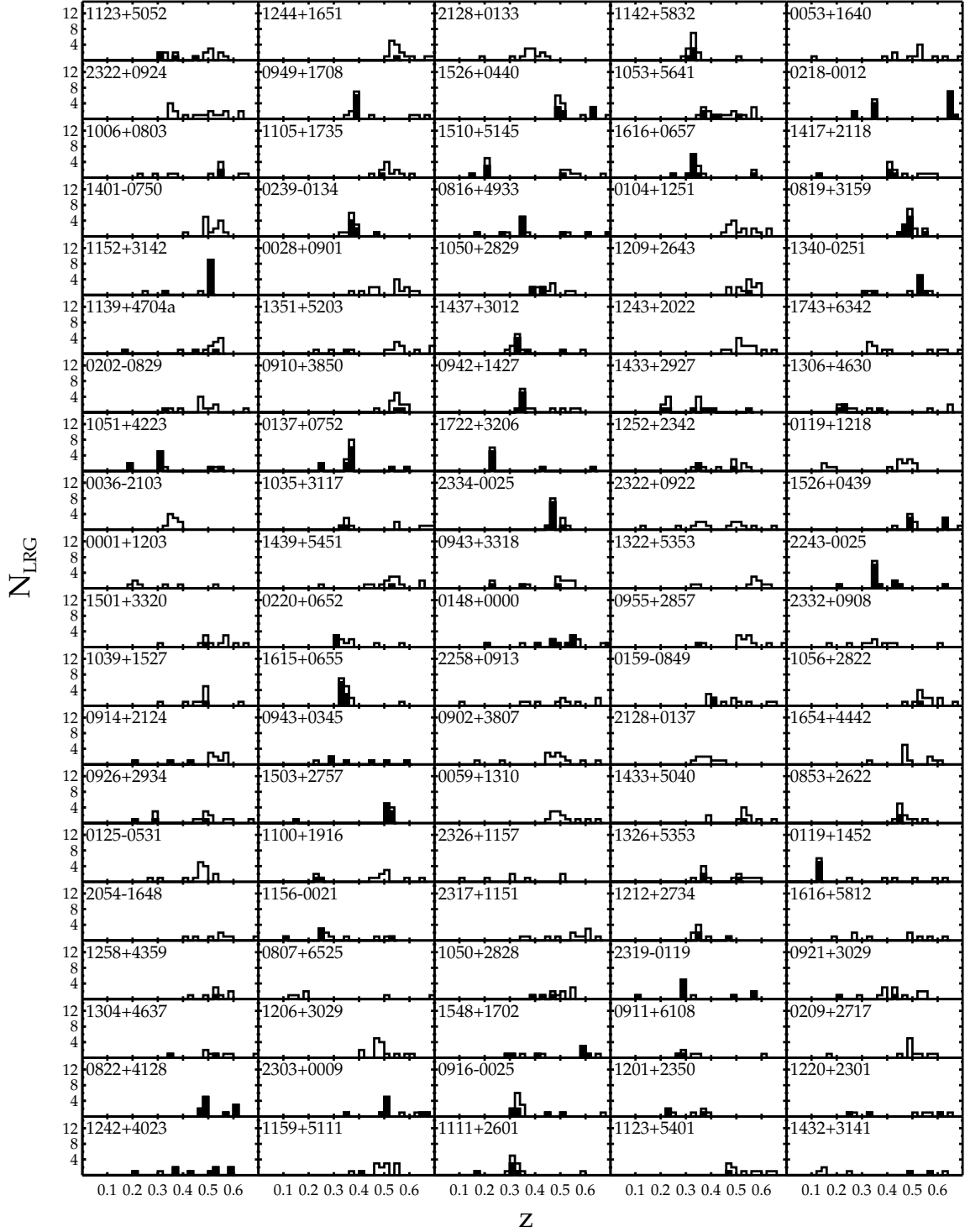


FIG. 6.— Same as Figure 4, but for our top 200 beams as ranked by total LRG luminosity. Our beams contain many more LRGs than the majority of the comparison sample of Hennawi and CLASH lensing clusters. Five of the Hennawi/CLASH clusters are recovered here (although our beams may be centered at different coordinates that include more LRGs). Our beams show a diversity of configurations, with some beams dominated by a single massive structure and others having multiple structures distributed throughout redshift space. Even single LRGs can trace massive lensing clusters (see Figure 4).

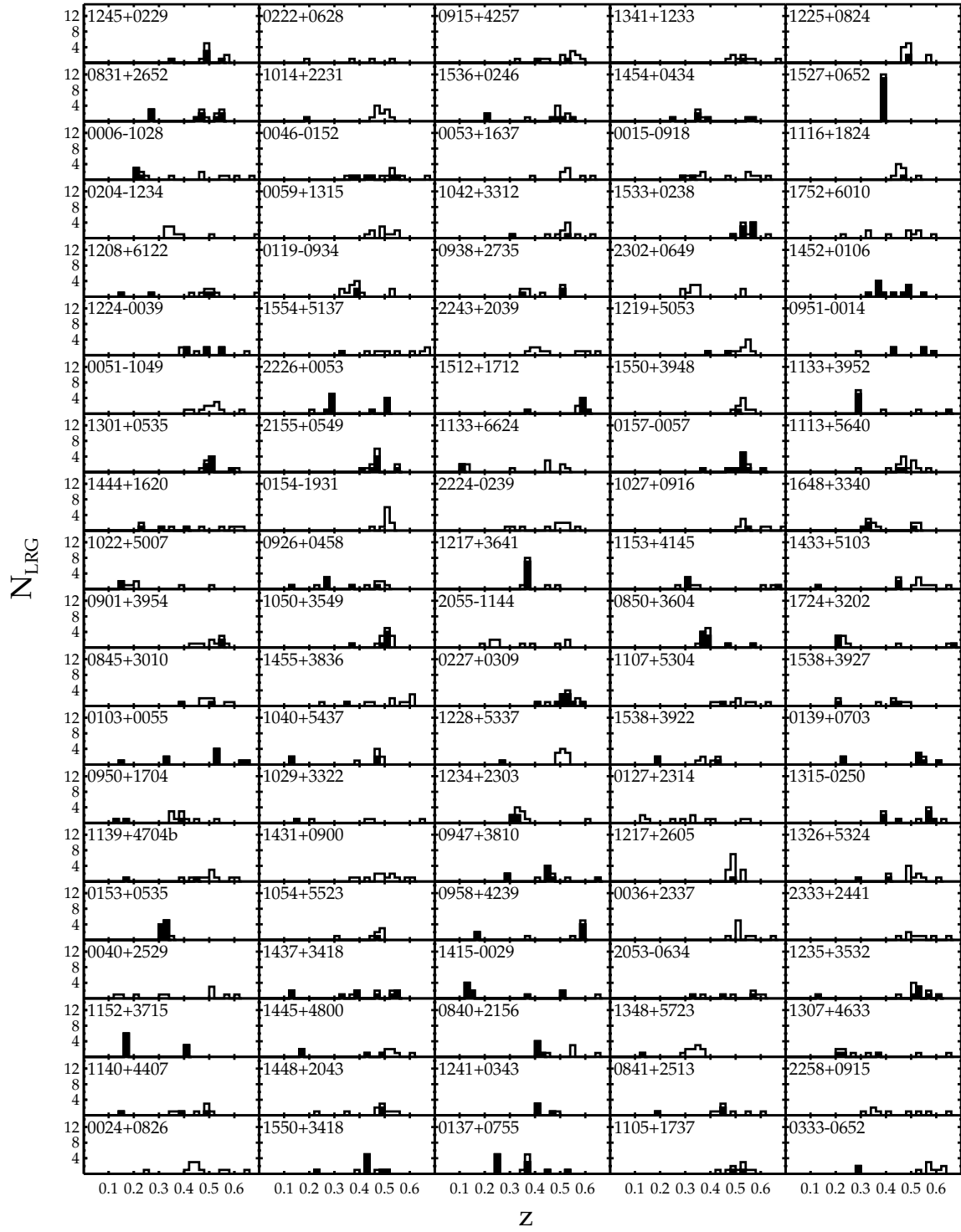


FIG. 6.— (Continued.)

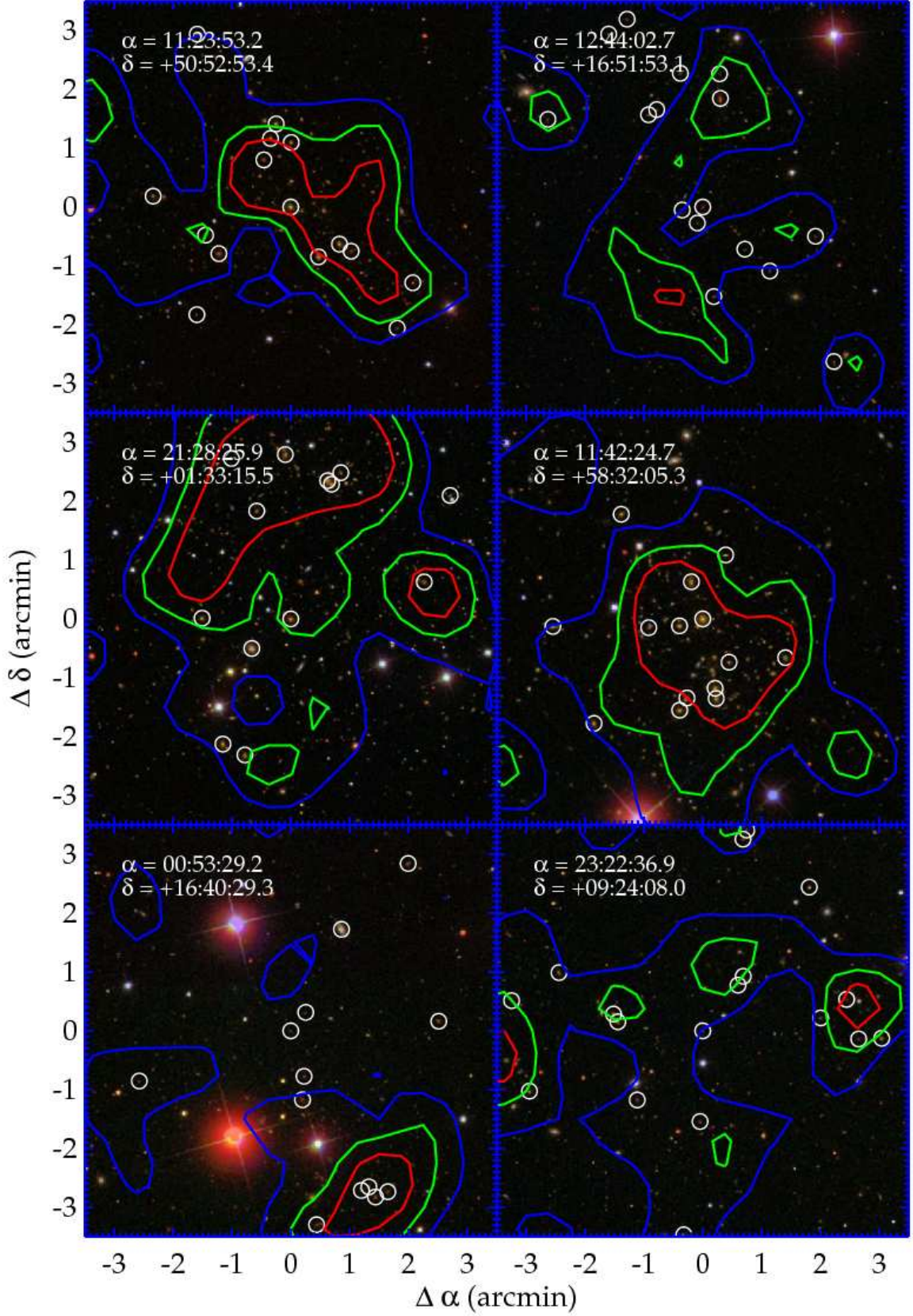


FIG. 7.— SDSS DR9 SkyServer images of the top 20 beams selected from the SDSS. Each panel is $7' \times 7'$ on a side. Each LRG in the field is indicated by a white circle. The contours enclose the projected overdensities of galaxies from the SDSS primary photometric galaxy catalog from the highest (red) to lowest (blue) projected overdensities. The coordinates of the beam center are given in the upper left corner of each panel. LRGs generally trace the overdensities. Like the redshift histograms, the projected galaxy densities in these fields show a variety of configurations, with some beams dominated by a single concentration of galaxies and others comprising multiple structures in projection.

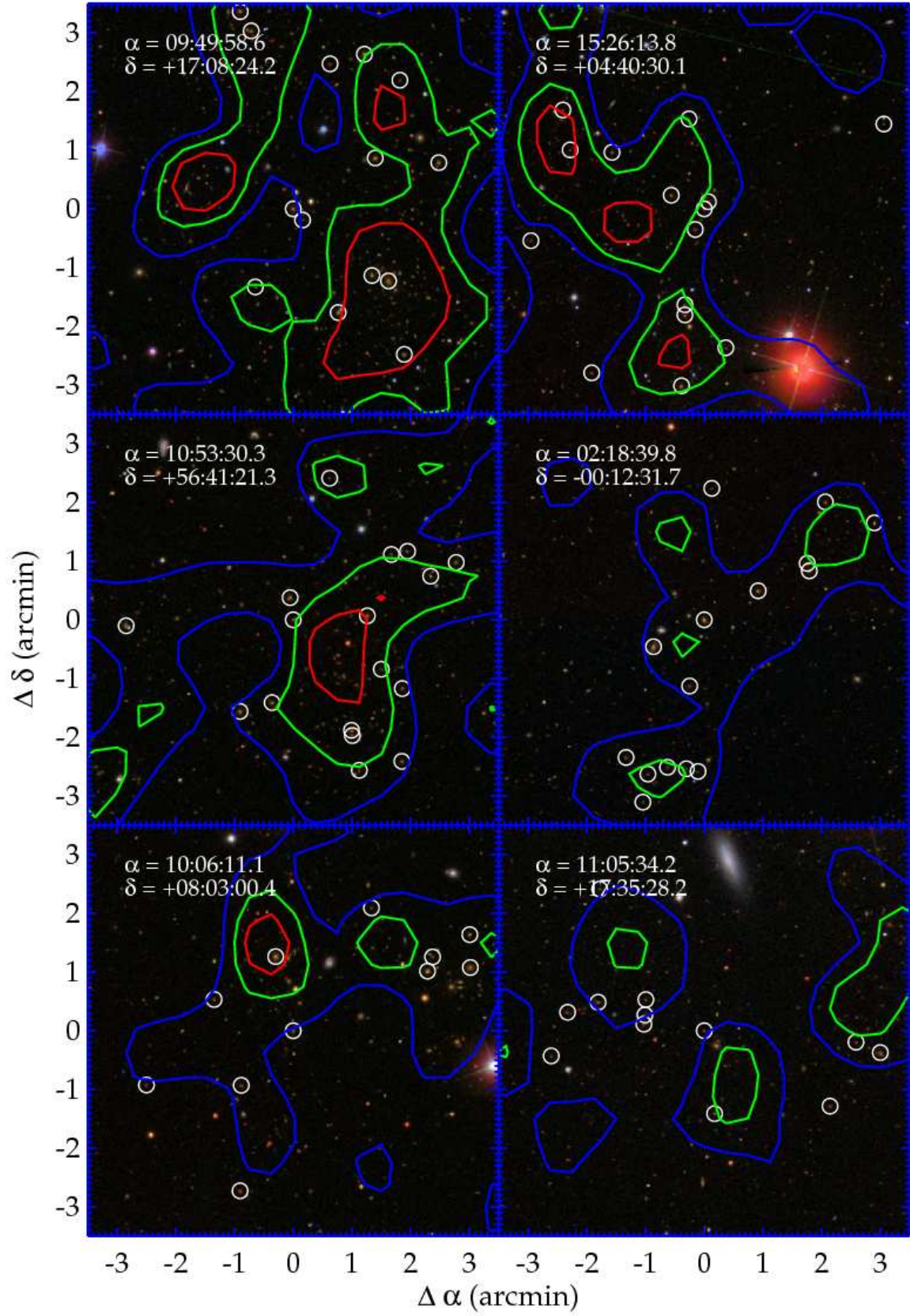


FIG. 7.— (Continued.)

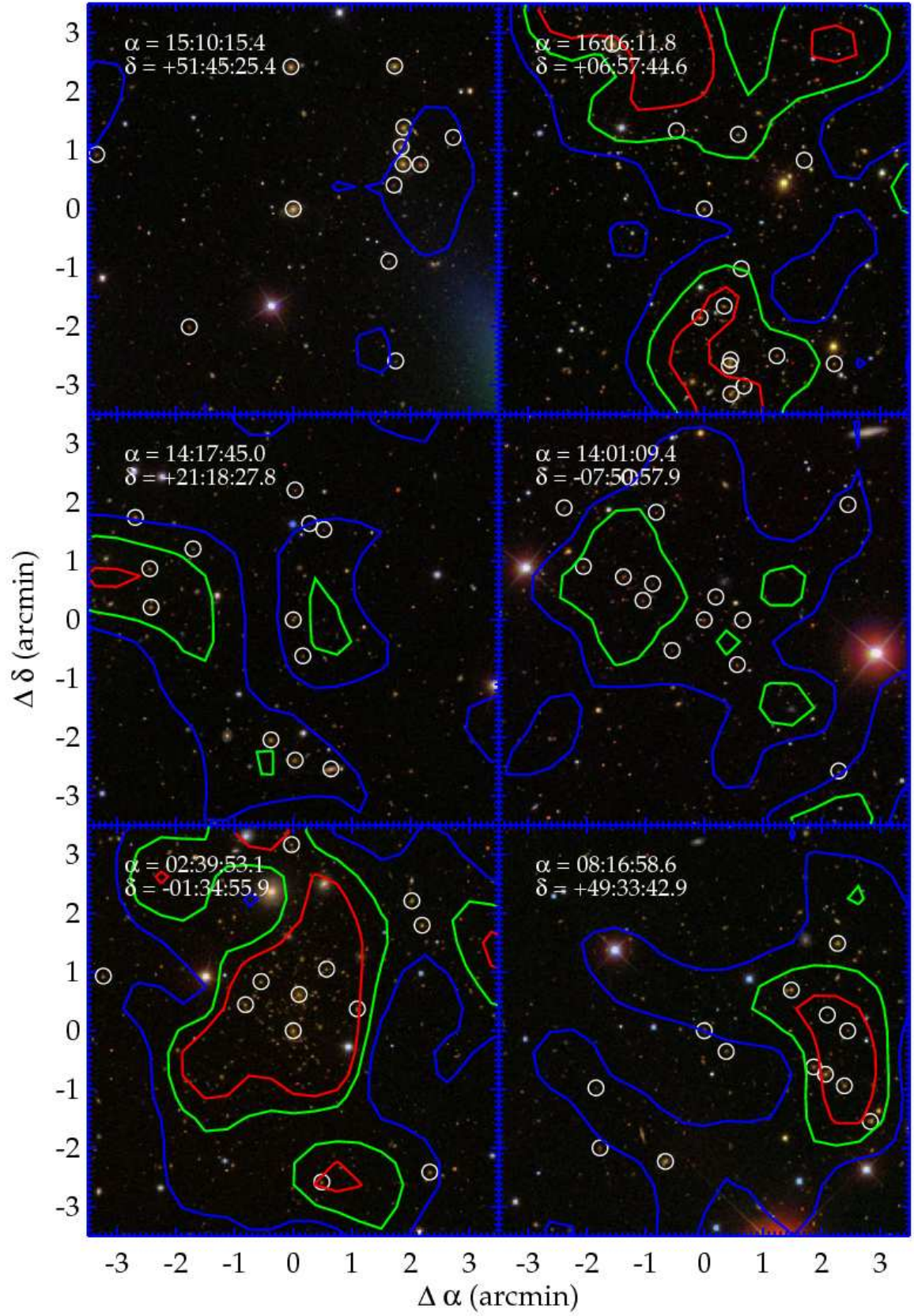


FIG. 7.— (Continued.)

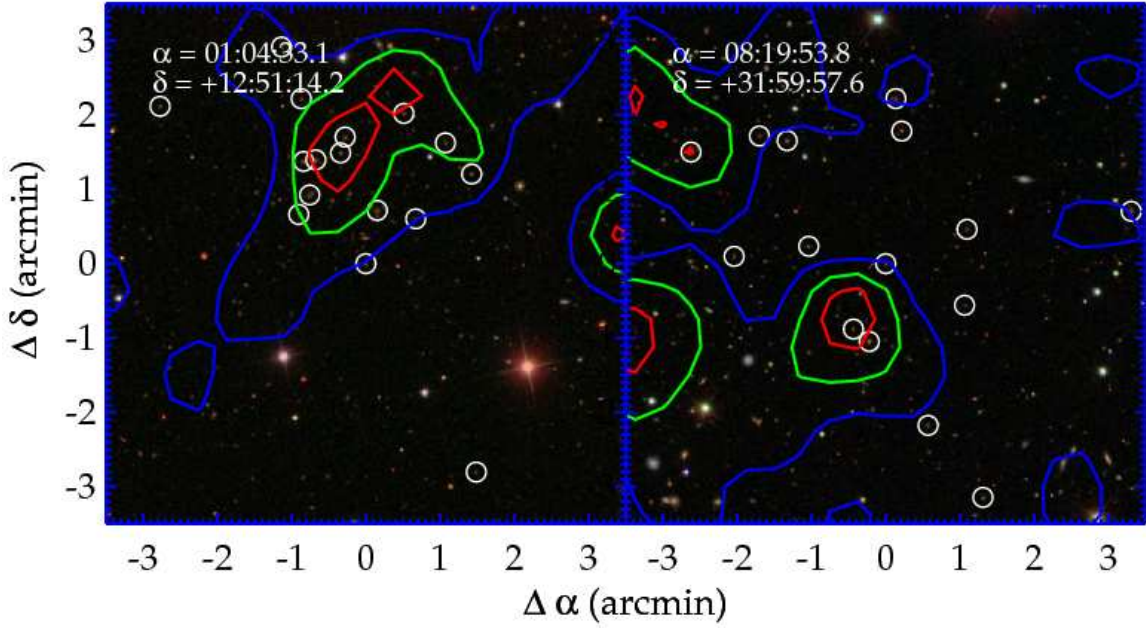


FIG. 7.— (Continued.)

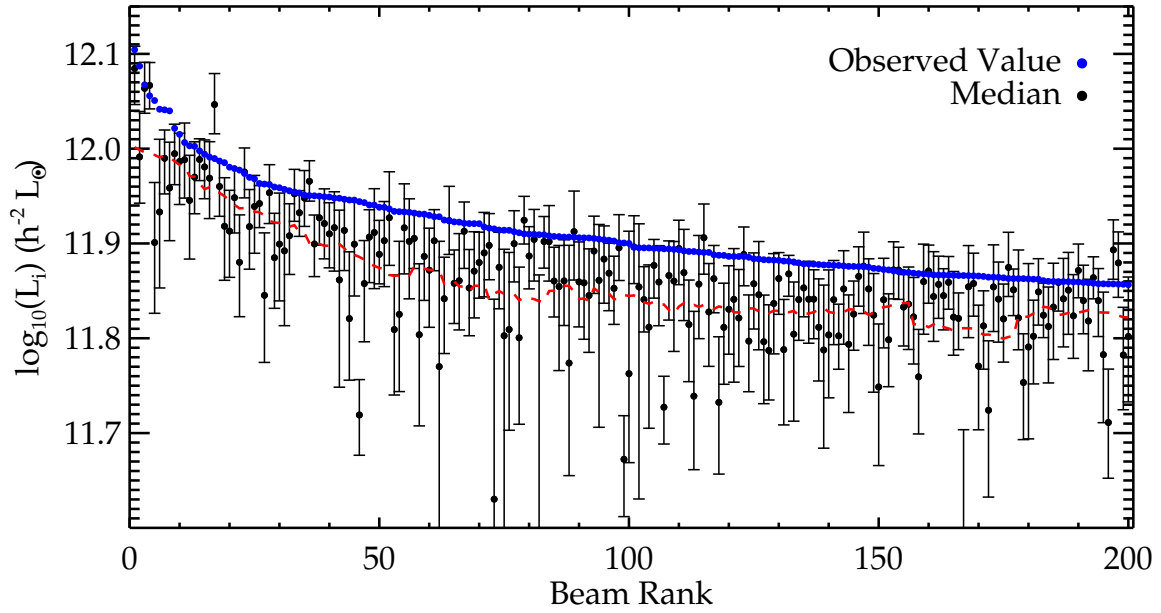


FIG. 8.— Integrated LRG luminosity as a function of beam rank for the top 200 beams. The observed value is given by the blue points. The black points represent the median total LRG luminosity over 1000 Monte Carlo realizations of each beam. The error bars represent the 16% and 84% quantiles of the luminosity distributions. The red dashed line is the 20-beam central moving average of the median Monte Carlo luminosities. The median luminosities are generally lower than the measured values due to expected biases when selecting the top-ranked beams, although the values still noticeably trend downward with increasing beam rank. When the top 1000 beams are re-ranked by the median integrated LRG luminosities over 200 trials per beam, $\sim 70 - 75\%$ of the beams within the top N beams, where $N \leq 200$, remain within the top N beams, showing that our beam selection is stable over this range.

and planned wide-area photometric and spectroscopic surveys. Ideally, we want a deeper survey than SDSS to probe a volume-limited sample of LRGs to higher redshift ($z \sim 1$) so as to include any cluster-scale lenses at $0.7 \lesssim z \lesssim 1$. However, any further observing time would be better utilized by expanding the survey area rather than going much deeper in redshift, as the number density of massive cluster-scale halos is decreasing at higher redshift (e.g., Tinker et al. 2008) and the lensing geometry for magnifying $z \geq 7$ galaxies is becoming unfavorable.

Surveys with goals that include detection of weak gravitational lensing, with their wide field of view, deep accurate multi-band photometry (particularly for cosmic magnification/convergence studies, e.g., Van Waerbeke et al. 2010; Hildebrandt et al. 2011; Ford et al. 2012), and accurate photometric redshifts, are promising for our selection method. Current examples include the Kilo-Degree Survey (KiDS; de Jong et al. 2013) and the complementary VISTA Kilo-degree Infrared Galaxy Survey (VIKING), as well as the 3π survey with the Panoramic Survey Telescope and Rapid Response System (Pan-STARRS; Kaiser 2004). The ongoing Dark Energy Survey (DES) will provide deep coverage in the southern sky, complementary to the SDSS coverage. Planned wide-field instruments and observatories, such as the Hyper Suprime-Cam on Subaru and the Large Synoptic Survey Telescope (LSST), will probe large areas of the sky to unprecedented depths and thus produce excellent datasets for our method. Space-based missions such as Euclid (Laureijs et al. 2011) and the Wide-Field Infrared Survey Telescope (WFIRST) will generate deep high-resolution photometry over a large fraction of the sky.

Spectroscopic surveys have the advantage of more robust LRG selection and more accurate redshifts (and therefore luminosities). A spectroscopic survey with sufficient resolution can also provide information on the physical clustering of the LRGs, which can lead to higher-order estimates of the underlying matter distribution. Because LRGs are ideal targets for studies of the baryon acoustic oscillation (BAO) feature (e.g., Eisenstein et al. 2005), the goals of BAO surveys match up well with searches for massive beams using our selection method. Spectra from the ongoing Baryon Oscillation Spectroscopic Survey (BOSS; Dawson et al. 2013), a fraction of which are included in the DR9 sample used here, will provide deep spectroscopic data across large areas of the sky and specifically target LRGs. The upcoming Big Baryon Oscillation Spectroscopic Survey (BigBOSS) will also achieve these goals and probe to deeper redshifts.

4. CONCLUSIONS

We present a new method of selecting lines of sight (“beams”) that contain large total masses and are likely to be the most powerful gravitational lenses for magnifying very high-redshift galaxies. These fields are important for studying the first galaxies, as their extreme lensing strengths can magnify the background source population into detectability. We select fields based on the total luminosity in luminous red galaxies (LRGs; e.g., Eisenstein et al. 2001) along the line of sight.

We identify the 200 lines of sight in the SDSS DR9 that

have the highest total LRG luminosities projected within a radius of $3.5'$ and within $0.1 \leq z \leq 0.7$, a key redshift range for lensing high-redshift galaxies. The total luminosities of LRGs in these fields ($\sim 10^{11.85} - 10^{12.1} h^{-2} L_{\odot}$), which can include 4 – 18 total LRGs, are 2 – 3 times larger than those of most known strong lensing galaxy clusters from the Hennawi et al. (2008) and CLASH (Postman et al. 2012) surveys, suggesting that they contain larger total masses. In those beams with multiple LRG peaks in redshift space, those peaks can be individually as rich as known lensing clusters, which may only be traced by a few LRGs.

The distribution of LRGs in these fields, both along the line-of-sight and in projection on the sky, show a diversity of structure. The LRGs trace both the redshift and angular concentrations of non-LRG galaxies. Some beams are dominated by a single mass peak, while others contain multiple mass peaks distributed along the line of sight, which can maximize the source plane area that is highly magnified for the purpose of detecting high-redshift galaxies (Wong et al. 2012). Visual inspection of the fields reveals many beams with obvious galaxy clusters, confirming that the LRGs do trace dense structures. 22.5% of the top 200 beams contain one known cluster and 56.0% contain multiple known clusters previously identified in the literature. The rest of the beams may contain new groups and clusters.

Our analysis of the uncertainties in the integrated LRG luminosities of these beams shows that while the detailed rankings are susceptible to fluctuations, the top 200 beams generally comprise fields that have large concentrations of massive galaxies. 70 – 75% of the beams remain in the top 200 when an extended sample of the top 1000 beams is sorted by the median LRG luminosity derived by our Monte Carlo error analysis, which accounts for uncertainties in the individual LRG luminosities and for galaxies falling into or out of our selection criteria.

Our follow-up galaxy spectroscopy in a subset of these beams has revealed multiple massive halos and large total masses ($\gtrsim 2 \times 10^{15} h^{-1} M_{\odot}$), confirming the power of using LRGs as tracers of massive structure (S. M. Ammons et al. 2013, in preparation). We are modeling the mass distributions in these beams from the spectroscopy alone, but will eventually combine that analysis with a strong lensing analysis of the arcs detected in these fields. The large total masses and multiple projected massive clusters make these beams likely to be among the best gravitational lenses known. Future science applications include the detection of faint lensed $z \geq 7$ galaxies that can be followed-up spectroscopically, high spatial resolution studies of strongly lensed galaxies at $z \sim 1 - 3$, weak lensing studies, and improved detections of γ -ray sources and supernovae at cosmological distances.

We thank Decker French for her contributions to this project. We are particularly indebted to Daniel Eisenstein and Nikhil Padmanabhan for useful discussions regarding the LRG selection criteria. We also thank Leon Baruah, Michael Blanton, Marcello Cacciato, Shirley Ho, Daniel Marrone, Jeremiah Ostriker, Ashley Ross, Jeremy Tinker, and Adi Zitrin for helpful discussions and input. This work was supported by NSF grants AST-0908280 and AST-1211385 and NASA grants ADAP-

NNX10AD476 and ADAP-NNX10AE88G. This work performed in part under the auspices of the U.S. Department of Energy by Lawrence Livermore National Laboratory under Contract DE-AC52-07NA27344. A.I.Z. thanks the Max Planck Institute for Astronomy and the Center for Cosmology and Particle Physics at New

York University for their hospitality and support during her stays there. This research has made use of the NASA/IPAC Extragalactic Database (NED), which is operated by the Jet Propulsion Laboratory, California Institute of Technology, under contract with the National Aeronautics and Space Administration.

APPENDIX

A. SORTING BY NUMBER OF LRGS VS TOTAL LRG LUMINOSITY

In selecting beams likely to contain large total masses as traced by LRGS, we choose to use total LRG luminosity rather than simple number counts, despite the fact that there are additional uncertainties associated with this method. This choice arises from the expectation that LRG luminosity traces stellar mass, which is related to halo mass. While there have not been quantitative studies of the relationship between halo mass and total LRG luminosity at the halo masses we are interested in, we run a simple test here to see whether total LRG luminosity or number counts in galaxy clusters provides a better contrast relative to the field population, i.e., a stronger measure of overdensity. We can then invoke the known relationship between halo mass and LRG number counts (Ho et al. 2009) to suggest that either total LRG luminosity or number counts is a better tracer of halo mass. We use early-type galaxy luminosity functions to compare the expected galaxy luminosity and number counts in beams containing a massive cluster and field galaxies to beams with field galaxies alone.

Adopting the *i*-band luminosity function (LF) of Bernardi et al. (2003) to represent the field population of LRGS, we calculate the number of galaxies within $0.1 \leq z \leq 0.7$ and brighter than $M_i - 5\log_{10}(h) \leq -21$ expected in a circular field of view of radius $3'5$. We then take the cluster galaxy *i*-band luminosity function of Popesso et al. (2005) to represent the population of LRGS in clusters. We use the Popesso et al. (2005) LF constraints for a cluster-centric radius $r \leq 2.0 h^{-1}$ Mpc with local background subtraction, although our results are qualitatively similar using their results for different cluster-centric radii. We combine the Popesso et al. (2005) bright-end and faint-end components into a single LF, although in practice, the faint-end component contributes very little at the luminosities we are interested in. Both the field and cluster samples are based on $z < 0.3$ LFs from SDSS data, so evolution in the LF is not taken into account, but both the field and cluster galaxy LFs will have smaller normalizations at higher redshifts.

We integrate the cluster LF down to the chosen limiting magnitude to determine a normalization factor, then normalize the cluster LF for a range of cluster richness, defined as the number of LRGS in the cluster. Since the Popesso et al. (2005) analysis ignored the contribution of the brightest cluster galaxy (BCG) when computing the LF, we add its contribution separately. We identify the luminosity at which the integrated LF is equal to one galaxy and double the differential number counts in the LF bins brighter than that luminosity. This effectively modifies the integral of the LF such that there is one additional galaxy in the cluster with the same average luminosity as its brightest (non-BCG) member. This is conservative in the sense that we will underestimate the luminosity of the BCG since there is a known magnitude gap between the two brightest galaxies in clusters (e.g., More 2012).

For a range of cluster richness, we compare number counts and total luminosity for the field plus cluster to those for the field alone. We define the number of LRGS in the field to be

$$N_{field} = \left(\frac{\pi R^2}{4\pi \text{ ster}} \right) \int_{z_{min}}^{z_{max}} (c/H(z))(1+z)^2 D_A(z)^2 dz \int_{L_{min}}^{\infty} \phi_{field}(L) dL, \quad (A1)$$

where R is the beam radius, $c/H(z)$ is the Hubble distance at redshift z , D_A is angular diameter distance, and $\phi_{field}(L)$ is the luminosity function for the field. The total luminosity for galaxies in the field is then given by

$$L_{field} = \left(\frac{\pi R^2}{4\pi \text{ ster}} \right) \int_{z_{min}}^{z_{max}} (c/H(z))(1+z)^2 D_A(z)^2 dz \int_{L_{min}}^{\infty} \phi_{field}(L) L dL. \quad (A2)$$

For the cluster galaxies, we define $N_{cluster}$ to be the number of non-BCG galaxies in the cluster. The total cluster richness is therefore $N_{cluster} + 1$, and the total luminosity of the cluster galaxies as a function of richness is

$$L_{cluster}(N_{cluster} + 1) = \frac{N_{cluster} \int_{L_{min}}^{\infty} (1 + \mathcal{H}(L - L_{BCG})) \phi_{cluster}(L) L dL}{\int_{L_{min}}^{\infty} \phi_{cluster}(L) dL}, \quad (A3)$$

where $\phi_{cluster}(L)$ is the luminosity function for the cluster with arbitrary normalization. The factor of $N_{cluster} / \int_{L_{min}}^{\infty} \phi_{cluster}(L) dL$ serves to normalize the total luminosity for the given richness. The $1 + \mathcal{H}(L - L_{BCG})$ term, where \mathcal{H} is the Heaviside step function, accounts for the luminosity of the BCG. L_{BCG} is determined by solving the equation

$$\int_{L_{BCG}}^{\infty} \phi_{cluster}(L) dL = \frac{\int_{L_{min}}^{\infty} \phi_{cluster}(L) dL}{N_{cluster}} \quad (A4)$$

for L_{BCG} . Note that the arbitrary normalization of the cluster LF cancels on both sides of Equation A4.

We assume $R = 3'.5$, $z_{min} = 0.1$, $z_{max} = 0.7$, and test a range of luminosity cuts from $-22.5 \leq M_{min} - 5\log_{10}(h) \leq -21$, where $M_{min} = -2.5\log_{10}(L_{min}/L_{\odot})$. We then define the “richness contrast” to be

$$C_N(N_{cluster} + 1) = \frac{N_{field} + N_{cluster} + 1}{N_{field}}, \quad (\text{A5})$$

and the “luminosity contrast” to be

$$C_L(N_{cluster} + 1) = \frac{L_{field} + L_{cluster}(N_{cluster} + 1)}{L_{field}}. \quad (\text{A6})$$

These contrasts represent the relative LRG number and luminosity, respectively, of a beam containing a cluster and field galaxies to a beam containing field galaxies alone. In general, while both richness and total luminosity are strongly correlated, the luminosity contrast is stronger than the number contrast, increasing with greater cluster richness. As an example, for a richness of $N_{cluster} + 1 = 12$ and L_{min} corresponding to a limiting magnitude of $M_i - 5\log_{10}(h) = -21$, C_L is 16% greater than C_N . Reid & Spergel (2009) find the LRG occupation number for $\gtrsim 10^{15}M_{\odot}$ halos to be $\sim 3 - 5$ LRGs, although their LRG selection was limited to more luminous LRGs than our sample. We test a range of limiting absolute magnitudes, $-21 \leq M_i - 5\log_{10}(h) \leq -22.5$, and find that the contrast for both methods becomes much greater for brighter limiting magnitudes.

For this test, we attempt to be conservative where possible. The magnitude gap for BCGs, which we ignore, would favor the luminosity method more by increasing the cluster luminosity. The field early-type LF is based on morphological+spectral PCA criteria, and almost certainly includes more galaxies than would pass our LRG selection criteria. This effect serves to reduce both contrasts, but given our finding that the luminosity contrast is stronger than the richness contrast, the luminosity contrast will be more strongly affected.

In Table 2, we list the $3'.5$ -radius beams containing ≥ 11 LRGs that do not overlap with the top 200 luminosity-sorted beams in Table 1. We present these beams for completeness, as these beams would have been in the top 200 (or had an equal number of LRGs to beams in our top 200) if we had chosen to sort by LRG number counts instead.

TABLE 2
LIST OF UNIQUE BEAMS SORTED BY N_{LRG}

RA	Dec	N_{LRG}	$\log_{10}(L_i)^a$ ($h^{-2} L_{\odot}$)
11:09:15.977	+09:57:53.352	13	11.85
13:38:26.535	+15:19:27.495	13	11.84
11:32:31.050	+36:50:53.636	13	11.84
10:05:55.896	+47:21:15.407	13	11.83
08:25:51.875	+40:16:59.830	13	11.82
16:28:13.439	+38:24:47.224	13	11.82
13:49:59.719	+39:33:59.337	13	11.80
10:02:39.789	+20:29:22.063	12	11.86
09:57:38.539	+19:38:45.942	12	11.85
15:11:05.994	+67:05:11.986	12	11.85
00:12:52.314	-08:57:47.332	12	11.85
14:54:20.869	+05:55:21.444	12	11.85
10:35:55.123	+59:06:58.574	12	11.85
16:32:14.530	+21:25:22.315	12	11.85
15:22:35.599	+42:34:42.615	12	11.84
08:53:30.710	+23:19:35.213	12	11.84
09:43:03.652	+47:01:14.102	12	11.84
16:27:27.221	+39:41:02.149	12	11.84
11:27:10.983	+20:44:39.185	12	11.84
10:30:35.164	+47:48:39.928	12	11.83
09:01:55.447	+20:54:16.831	12	11.83
09:08:49.813	+61:27:28.658	12	11.82
15:11:48.439	+13:52:02.737	12	11.82
14:15:18.477	+33:44:52.386	12	11.82
16:17:39.046	+42:32:45.143	12	11.82
11:32:52.075	+36:47:13.073	12	11.81
12:10:48.221	+60:17:41.794	12	11.81
22:43:20.719	-09:35:18.906	12	11.81
12:01:17.199	+14:55:49.153	12	11.81
15:42:25.294	+60:03:01.397	12	11.80
00:44:52.396	+07:05:47.833	12	11.79
09:53:34.737	+22:49:09.630	12	11.79
13:21:22.061	+05:59:07.882	12	11.79
01:38:45.981	-10:16:53.809	12	11.78
08:12:48.436	+52:19:06.964	12	11.78
11:03:04.694	+04:19:41.855	12	11.78
15:17:46.067	+04:47:01.250	12	11.77
15:48:22.764	+12:54:52.040	12	11.77
02:18:14.999	-17:04:18.076	12	11.77
02:39:02.368	-01:08:11.545	12	11.76
10:29:25.019	+23:17:29.250	12	11.76
17:28:37.980	+68:14:07.625	12	11.75
13:00:55.901	+22:30:43.953	12	11.74
11:47:43.158	+25:29:07.848	12	11.68
08:04:54.807	+40:26:23.249	11	11.86
12:31:28.851	+17:48:50.446	11	11.85
00:47:16.514	-01:45:44.736	11	11.85
20:54:49.076	-16:20:14.773	11	11.85
12:02:14.719	+61:42:10.414	11	11.85
14:56:43.695	+11:59:50.193	11	11.85

^aTotal integrated rest-frame i -band luminosity in LRGs.

TABLE 2
CONTINUED.

RA	Dec	N_{LRG}	$\log_{10}(L_i)^a$ ($h^{-2} L_{\odot}$)
14:39:20.170	+05:44:35.922	11	11.85
12:22:15.002	+42:34:30.585	11	11.85
09:28:38.426	+37:46:55.479	11	11.85
13:24:06.064	+47:40:26.833	11	11.84
23:11:48.346	+03:40:47.616	11	11.84
12:29:01.509	+47:38:55.367	11	11.84
15:39:40.493	+34:25:27.277	11	11.84
11:06:08.485	+33:33:39.682	11	11.84
12:38:51.513	+13:06:30.845	11	11.84
12:21:43.787	+45:25:05.301	11	11.84
11:59:31.823	+49:48:05.792	11	11.84
09:50:59.745	+00:39:43.027	11	11.84
13:24:11.822	+52:18:49.644	11	11.84
16:14:33.153	+62:40:58.110	11	11.84
21:35:24.074	-00:59:50.579	11	11.83
01:04:27.673	+29:03:36.591	11	11.83
08:53:03.792	+52:56:30.040	11	11.83
15:57:52.855	+21:33:41.153	11	11.83
16:28:17.576	+11:09:59.566	11	11.83
15:37:33.252	+28:06:36.831	11	11.83
09:49:12.774	+50:16:09.466	11	11.83
11:28:15.367	+25:49:22.565	11	11.83
00:06:56.132	-00:40:51.829	11	11.82
14:39:38.927	+05:44:00.469	11	11.82
01:01:40.797	+02:36:46.424	11	11.82
13:44:19.219	+39:06:38.980	11	11.82
11:15:59.327	+15:05:20.129	11	11.82
09:26:08.246	+04:25:26.035	11	11.82
13:59:49.878	+49:35:49.136	11	11.82
00:42:54.313	+27:26:47.716	11	11.82
14:18:21.801	+03:03:55.582	11	11.82
03:17:11.206	-07:13:09.000	11	11.82
08:52:49.102	+30:26:33.467	11	11.81
10:55:13.169	+43:57:56.860	11	11.81
08:34:13.159	+45:25:20.803	11	11.81
08:59:37.436	+26:05:36.539	11	11.81
14:09:04.402	+34:45:34.558	11	11.81
17:30:12.322	+55:52:30.416	11	11.81
23:16:25.189	-01:54:32.230	11	11.81
09:16:25.803	+29:52:07.585	11	11.81
09:27:37.817	+56:16:58.192	11	11.81
02:12:41.969	-09:42:27.342	11	11.81
14:59:34.701	+45:14:34.771	11	11.80
14:40:10.313	+14:17:11.818	11	11.80
14:45:18.655	+00:06:31.825	11	11.80
12:10:39.503	+04:29:20.492	11	11.80
23:05:50.195	+00:06:36.279	11	11.80
10:08:54.896	+45:27:58.888	11	11.80
11:51:54.536	+17:50:37.422	11	11.80
11:43:23.554	-00:28:01.790	11	11.80

TABLE 2
CONTINUED.

RA	Dec	N_{LRG}	$\log_{10}(L_i)^a$ ($h^{-2} L_{\odot}$)
10:21:25.938	+12:14:39.260	11	11.80
02:01:07.278	+13:22:24.961	11	11.80
13:29:24.519	+65:27:53.321	11	11.80
10:10:33.584	+08:07:05.982	11	11.80
13:01:50.667	+22:43:34.859	11	11.79
01:17:33.818	+15:45:48.878	11	11.79
15:43:29.983	+35:42:18.202	11	11.79
12:37:03.247	+27:58:19.516	11	11.79
11:13:14.638	+25:59:44.165	11	11.79
00:11:01.227	+29:07:51.757	11	11.79
11:49:13.307	+35:31:54.141	11	11.79
03:17:53.373	-07:05:31.346	11	11.78
11:12:15.720	+23:52:40.054	11	11.78
00:33:20.715	+04:16:19.676	11	11.78
23:31:26.943	+00:35:06.526	11	11.78
09:00:49.059	+38:29:12.213	11	11.78
22:58:51.623	-03:25:22.241	11	11.78
11:09:31.024	+09:55:00.194	11	11.77
01:02:46.991	+11:10:25.567	11	11.77
12:35:18.759	+41:19:56.381	11	11.77
09:27:22.794	+44:10:08.169	11	11.76
00:00:52.090	+28:09:08.009	11	11.76
00:46:16.731	-10:24:23.642	11	11.76
12:46:24.192	+36:26:12.921	11	11.76
14:27:36.058	+55:49:26.812	11	11.76
01:13:15.628	+28:20:05.420	11	11.75
12:06:09.519	+44:41:04.943	11	11.75
23:04:24.257	+02:12:24.002	11	11.74
09:41:17.904	+18:46:46.990	11	11.74
14:20:58.067	+21:08:07.372	11	11.74
10:31:48.173	+47:22:24.694	11	11.74
13:10:56.248	+45:15:35.924	11	11.74
09:27:59.505	+12:45:50.494	11	11.73
10:33:29.650	+37:13:26.586	11	11.73
14:18:21.330	+48:37:36.040	11	11.73
12:50:52.163	+26:49:38.982	11	11.73
15:20:25.556	+06:21:48.889	11	11.72
12:26:50.804	+33:11:20.101	11	11.72
12:41:02.456	+44:12:13.803	11	11.72
16:07:35.906	+16:51:04.155	11	11.72
02:00:18.811	-07:54:08.177	11	11.71
11:54:30.316	+05:24:40.867	11	11.71
14:03:39.841	+10:14:54.200	11	11.71
11:38:25.361	+27:02:21.213	11	11.70
11:48:32.089	+37:48:31.262	11	11.70
11:47:25.348	+44:20:02.282	11	11.69
14:01:18.524	+15:14:08.027	11	11.68
14:31:57.545	+06:37:21.361	11	11.67
11:09:37.592	+38:28:53.623	11	11.65

```

SELECT
  g.objID,
  g.run,
  g.rerun,
  g.camcol,
  g.field,
  g.fieldID,
  g.obj,
  g.ra,
  g.dec,
  g.b,
  g.dered_g,
  g.dered_r,
  g.dered_i,
  g.extinction_r,
  g.petroMag_r,
  g.psfMag_r,
  g.ModelMag_r,
  g.ModelMagErr_r,
  g.psfMag_i,
  g.ModelMag_i,
  g.ModelMagErr_i,
  g.deVRad_r,
  g.petroR50_r,
  g.flags,
  p.z,
  p.zErr,
  f.quality,
  f.psfWidth_r

FROM
  Galaxy as g, Photoz as p, Field as f

WHERE p.objID = g.objID
  and f.fieldID = g.fieldID
  and f.quality = 3
  and f.psfWidth_r < 2
  and (g.dered_g - g.dered_r) < 3.0
  and (g.dered_r - g.dered_i) < 1.5
  and g.extinction_r < 0.2
  and g.modelmagerr_r < 0.2
  and (g.petroMag_r + (2.5 * LOG10(2 * pi() * POWER(g.petroR50_r,2.0)))) < 24.2
  and ABS(g.b) > 30
  and ABS((g.dered_r - g.dered_i) - ((g.dered_g - g.dered_r) / 4.0) - 0.18) < 0.2
  and (g.petroMag_r - g.extinction_r) <
    (13.6 + ((0.7 * (g.dered_g - g.dered_r)) + (1.2 * (g.dered_r - g.dered_i - 0.18))) / 0.3)
  and (g.petroMag_r - g.extinction_r) < 19.7
  and (g.psfMag_r - g.ModelMag_r) > 0.3
  and (g.flags & 0x0000000000000002) = 0
  and (g.flags & 0x0000000000000004) = 0
  and (g.flags & 0x0000000000000008) = 0
  and (g.flags & 0x0000000000004000) = 0
  and (g.flags & 0x0000000000100000) = 0
  and (g.flags & 0x0000000002000000) = 0
  and (g.flags & 0x0000000004000000) = 0
  and (g.flags & 0x0000000070000000) != 0

```

FIG. 9.— SDSS database SQL query for Cut I.

B. SDSS LRG SELECTION CRITERIA

In this Appendix, we explain our LRG catalog selection criteria. We base our selection of SDSS DR9 LRGs on the criteria originally defined in Padmanabhan et al. (2005), with some minor modifications. The LRG selection uses two separate selection criteria (denoted “Cut I” and “Cut II” for the $z \lesssim 0.4$ and $z \gtrsim 0.4$ samples, respectively) to define the full sample. The SQL queries for the two cuts are given in Figures 9 and 10. The two cuts are not mutually exclusive, so we remove duplicate objects after combining the two samples into a single catalog.

We modify the original LRG selection criteria, which selected LRGs for clustering studies that had different requirements than our applications. We add cuts to exclude fields with poor quality or that have an effective r -band PSF width $\geq 2''$, indicating poor seeing. We remove objects with r -band extinction ≥ 0.2 or r -band magnitude errors ≥ 0.2 , as we are less confident in these objects’ absolute magnitudes (N. Padmanabhan, private communication). We reduce the galactic latitude criterion from $b \leq 45^\circ$ to $b \leq 30^\circ$, which strikes a balance between excluding fields with a high-density of stars that could complicate follow-up observations and including as much survey area as possible. This cut eliminates less than 20% of the total sky coverage of DR9. The rest of our color and photometric flag cuts remove most spurious stellar contaminants. The photometry flags are standard quality cuts to remove spurious objects (A. Ross, private communication). Based on a visual inspection of subsets of objects in our sample, we also cut objects with the “subtracted” or “deblended_as_psf” flags set, which removes $< 1\%$ of our sample but cuts out objects

```

SELECT
  g.objID,
  g.run,
  g.rerun,
  g.camcol,
  g.field,
  g.fieldID,
  g.obj,
  g.ra,
  g.dec,
  g.b,
  g.dered_g,
  g.dered_r,
  g.dered_i,
  g.extinction_r,
  g.petroMag_r,
  g.psfMag_r,
  g.ModelMag_r,
  g.ModelMagErr_r,
  g.psfMag_i,
  g.ModelMag_i,
  g.ModelMagErr_i,
  g.deVRad_r,
  g.petroR50_r,
  g.flags,
  p.z,
  p.zErr,
  f.quality,
  f.psfWidth_r

FROM
  Galaxy as g, Photoz as p, Field as f

WHERE P.objID = g.objID
  and f.fieldID = g.fieldID
  and f.quality = 3
  and f.psfWidth_r < 2
  and (g.dered_g - g.dered_r) < 3.0
  and (g.dered_r - g.dered_i) < 1.5
  and g.extinction_r < 0.2
  and g.modelmagerr_r < 0.2
  and (g.petroMag_r + (2.5 * LOG10(2 * pi() * POWER(g.petroR50_r,2.0)))) < 24.2
  and ABS(g.b) > 30
  and ((g.dered_r - g.dered_i) - ((g.dered_g - g.dered_r) / 8)) > 0.55
  and (g.dered_g - g.dered_r) > 1.4
  and g.dered_i < (18.3 + (2 * ((g.dered_r - g.dered_i) - (g.dered_g - g.dered_r) / 8)))
  and g.dered_i < 20
  and (g.psfMag_i - g.ModelMag_i) > 0.2 * (21 - g.dered_i)
  and g.deVRad_r > 0.2
  and (g.flags & 0x0000000000000002) = 0
  and (g.flags & 0x0000000000000004) = 0
  and (g.flags & 0x0000000000000008) = 0
  and (g.flags & 0x0000000000004000) = 0
  and (g.flags & 0x0000000000010000) = 0
  and (g.flags & 0x0000000000200000) = 0
  and (g.flags & 0x0000000004000000) = 0
  and (g.flags & 0x0000000070000000) != 0

```

FIG. 10.— SDSS database SQL query for Cut II.

contaminated by a nearby bright star. We also cut objects with the “deblend_pruned” flag set, which removes a tiny fraction (< 100 objects) of our sample with apparent blending issues.

We use similar criteria to get the spectroscopic sample of LRGs, requiring in addition that the “zwarning” flag is zero and the redshift error is $< 10^{-3}$. We then match the spectroscopic and photometric samples, replacing the photometric redshift and its error with the spectroscopic redshift and error where applicable. We apply cuts on the object redshift only after combining the catalogs, as an object with a photometric redshift outside of our target redshift range ($0.1 \leq z \leq 0.7$) may have a spectroscopic redshift within that range.

We then calculate absolute magnitudes for the LRGs, accounting for K-corrections and passive evolution, and apply our absolute i -band magnitude cut. We extend the original Padmanabhan et al. (2005) absolute magnitude cut ($-21 < M_i - 5\log_{10}(h) < -24$) to include more luminous galaxies up to -24.7 based on visual inspection. While extending this cut does introduce contaminants, it also includes the most luminous LRGs, which contribute the most to the total luminosity of a beam. We check through visual inspection that these contaminants do not affect our top 200 beams.

C. KNOWN CLUSTERS IN TOP 200 BEAMS

We present the list of known clusters in our top 200 beams in Table 3. These clusters were identified in a search of the NASA/IPAC Extragalactic Database⁸ (NED) as galaxy clusters within $3'.5$ of our beam centers⁹. The clusters in each beam are ordered by angular offset from the beam center.

⁸ <http://ned.ipac.caltech.edu>

⁹ Z. Wen reports in a private communication that most of our LRG-selected fields contain at least one cluster identified in his larger Wen et al. (2012) sample, which was not available through NED at the time of our analysis.

TABLE 3
LIST OF KNOWN CLUSTERS IN SDSS LRG BEAMS

Rank	RA	Dec	Cluster ^a	Redshift ^b
1	11:23:53.231	+50:52:53.458	WHL J112353.2+505253	0.332
			ZwCl 1121.0+5110	...
			GMBCG J171.03358+50.88460	0.416
2	12:44:02.713	+16:51:53.185	WHL J124359.7+16511	0.5593
			GMBCG J191.00805+16.83941	0.516
			GMBCG J191.02734+16.89091	0.486
			MS 1241.5+1710	0.312
4	11:42:24.777	+58:32:05.333	WHL J114224.8+583205	0.3109
			Abell 1351	0.3224
			GMBCG J175.58575+58.48567	0.211
7	09:49:58.602	+17:08:24.240	MACS J0949.8+1708	0.3826
			GMBCG J147.50544+17.11794	0.443
			GMBCG J147.52556+17.13526	0.537
			WHL J094951.3+170701	0.3638
			GMBCG J147.47303+17.18400	0.39
8	15:26:13.832	+04:40:30.109	GMBCG J231.56702+04.67892	0.499
			WHL J152612.1+043951	0.5169
9	10:53:30.330	+56:41:21.327	WHL J105325.2+564042	0.4571
			GMBCG J163.33806+56.69041	0.4
			GMBCG J163.40388+56.66324	0.406
10	02:18:39.886	-00:12:31.752	SDSS CE J034.664303-00.205654	0.31075
			WHL J021843.3-001259	0.3483
			WHL J021845.2-001452	0.6338
11	10:06:11.170	+08:03:00.487	WHL J100601.9+080401	0.27275
			GMBCG J151.49575+08.06809	0.38
12	11:05:34.246	+17:35:28.209	WHL J110538.5+173544	0.5038
			WHL J110521.7+173505	0.5099
14	16:16:11.888	+06:57:44.695	GMBCG J244.03332+06.98599	0.34248
			NSC J161620+065841	0.3357
			GMBCG J244.07472+06.91786	0.408
			WHL J161609.9+065437	0.3288
			GMBCG J244.07577+07.00922	0.255
15	14:17:45.068	+21:18:27.860	GMBCG J214.44457+21.27367	0.409
			WHL J141755.5+211840	0.4023
			GMBCG J214.48589+21.33680	0.429
17	02:39:53.126	-01:34:55.980	Abell 370	0.375
18	08:16:58.695	+49:33:42.953	GMBCG J124.19153+49.54958	0.387
			WHL J081644.7+493512	0.3349
20	08:19:53.827	+31:59:57.660	WHL J081955.9+315904	0.5086
			GMBCG J125.00893+31.96433	0.318
			GMBCG J125.02582+32.02435	0.419
21	11:52:08.844	+31:42:35.278	WHL J115203.0+314100	0.5353
			WHL J115204.5+314458	0.4883
			WHL J115202.8+314516	0.349
23	10:50:03.460	+28:29:58.080	GMBCG J162.48938+28.51768	0.462
			GMBCG J162.50300+28.46881	0.389
			WHL J105005.2+283222	0.4335
			GMBCG J162.56190+28.50020	0.411
24	12:09:15.992	+26:43:33.237	WHL J120918.8+264101	0.5327
25	13:40:46.678	-02:51:50.541	WHL J134046.7-025150	0.532
26	11:39:26.649	+47:04:27.608	GMBCG J174.81035+47.03759	0.44
			WHL J113920.0+470727	0.5223
			GMBCG J174.78774+47.10125	0.323
27	13:51:32.691	+52:03:33.346	GMBCG J207.84562+52.06839	0.338
			WHL J135143.9+520407	0.3875

NOTE. — Galaxy clusters identified from NASA/IPAC Extragalactic Database (NED) within 3/5 of the beam centers. Clusters are sorted by proximity to the beam center. References – WHL = Wen et al. (2009); ZwCl = Zwicky et al. (1961); GMBCG = Hao et al. (2010); MS = Ueda et al. (2001); Abell = Abell et al. (1989); MACS = Ebeling et al. (2001); NSC = Gal et al. (2003); EAD = Estrada et al. (2007); MaxBCG = Koester et al. (2007); NSCS = Lopes et al. (2004); SDSS CE = Goto et al. (2002); SHELS = Geller et al. (2005); AWM = Abate et al. (2009); DDM = Desai et al. (2004)

^aFor clusters with multiple designations, we list the first designation given by NED.

^bRedshift precision to lowest significant non-zero digit.

TABLE 3
CONTINUED.

Rank	RA	Dec	Cluster ^a	Redshift ^b
28	14:37:40.295	+30:12:00.275	WHL J143740.3+301200	0.3271
			Abell 1943	0.182
			NSC J143737+300923	0.338
29	12:43:08.915	+20:22:51.768	GMBCG J190.77072+20.34803	0.418
			GMBCG J190.77001+20.41813	0.504
			WHL J124307.6+202537	0.5044
30	17:43:22.152	+63:42:57.575	WHL J174330.4+634141	0.3211
			Abell 2280	0.326
			NSC J174255+634144	0.3606
31	02:02:01.333	-08:29:02.252	WHL J020155.8-082720	0.4836
			WHL J020212.0-082849	0.3705
			GMBCG J030.46031-08.47258	0.305
			GMBCG J030.53418-08.43703	0.349
32	09:10:41.968	+38:50:33.710	GMBCG J137.68624+38.83708	0.511
			WHL J091049.8+385009	0.5651
			GMBCG J137.69226+38.79387	0.415
33	09:42:55.372	+14:27:20.611	WHL J094253.2+142907	0.3335
			GMBCG J145.73927+14.50789	0.346
34	14:33:25.780	+29:27:45.979	Abell 1934	0.2194
			GMBCG J218.35869+29.48397	0.354
			[EAD2007] 500	0.40968
			MaxBCG J218.32159+29.51165	0.22145
35	13:06:54.628	+46:30:36.691	WHL J130657.3+463206	0.2081
			Abell 1682	0.2339
			GMBCG J196.70832+46.55927	0.245
			NSC J130639+463208	0.2508
			GMBCG J196.75262+46.56389	0.337
36	10:51:34.352	+42:23:29.626	Abell 1110	0.194
			NSC J105128+422216	0.2982
			GMBCG J162.89536+42.34162	0.187
37	01:37:26.699	+07:52:09.305	GMBCG J260.55436+32.11438	0.304
			GMBCG J260.51908+32.07349	0.388
			GMBCG J260.61326+32.13257	0.225
38	17:22:13.049	+32:06:51.773	GMBCG J260.55436+32.11438	0.304
			GMBCG J260.51908+32.07349	0.388
			GMBCG J260.61326+32.13257	0.225
39	12:52:58.597	+23:42:00.034	WHL J125251.8+234206	0.3765
			WHL J125300.6+234414	0.5187
			ZwCl 1250.6+2401	...
			GMBCG J193.29269+23.66893	0.457
40	01:19:56.788	+12:18:34.735	NSCS J011959+121839	0.37
42	10:35:35.605	+31:17:47.478	NSCS J103537+311759	0.36
			GMBCG J158.90316+31.26230	0.332
			ZwCl 1032.9+3131	0.28085
			WHL J103527.2+312001	0.3702
			GMBCG J158.88440+31.35249	0.336
43	23:34:23.927	-00:25:00.606	SDSS CE J353.605194-00.417486	0.37883
			GMBCG J353.58053-00.42458	0.462
			WHL J233424.3-002618	0.4461
45	15:26:26.690	+04:39:04.707	GMBCG J231.56702+04.67892	0.499
46	00:01:58.481	+12:03:58.021	NSCS J000153+120347	0.2033
			Abell 2692	0.192
47	14:39:56.246	+54:51:14.221	WHL J143958.0+545031	0.5435
			MaxBCG J220.01388+54.80918	0.26465
			GMBCG J219.97530+54.80381	0.398
48	09:43:29.460	+33:18:49.403	NSC J094329+331912	0.2463
			ZwCl 0940.6+3334	...
			GMBCG J145.91018+33.31696	0.25655
			WHL J094339.7+332037	0.4815
			WHL J094316.0+331825	0.3216
50	22:43:28.058	-00:25:58.808	GMBCG J340.83815-00.43147	0.445
			WHL J224326.0-002405	0.3495
			GMBCG J340.82973-00.45495	0.184
51	15:01:56.456	+33:20:41.059	GMBCG J225.48502+33.33266	0.304
52	02:20:56.845	+06:52:09.157	NSCS J022059+065249	0.35

TABLE 3
CONTINUED.

Rank	RA	Dec	Cluster ^a	Redshift ^b
53	01:48:08.231	+00:00:59.692	GMBCG J027.04490+00.00106 SDSS CE J027.042007+00.011633	0.38 0.34479
56	10:39:51.501	+15:27:25.227	WHL J103952.8+152712 GMBCG J159.97959+15.45350 GMBCG J159.90661+15.44490	0.4893 0.285 0.496
57	16:15:59.965	+06:55:18.520	WHL J161609.9+065437	0.3288
59	01:59:59.711	-08:49:39.704	WHL J015951.0-084910 GMBCG J029.95560-08.83299 MACS J0159.8-0849	0.4032 0.322 0.405
60	10:56:14.771	+28:22:23.064	WHL J105614.8+282223 GMBCG J164.03905+28.37180	0.5731 0.478
61	09:14:23.778	+21:24:52.512	WHL J091424.2+212543 GMBCG J138.61986+21.41015	0.545 0.425
63	09:02:16.490	+38:07:07.073	GMBCG J135.52728+38.09073 WHL J090208.9+380450	0.492 0.4962
65	16:54:24.482	+44:42:10.793	WHL J165420.1+444125	0.4549
66	09:26:35.472	+29:34:22.128	WHL J092635.5+293422 ZwCl 0923.6+2946 WHL J092628.0+293452 GMBCG J141.61858+29.59521 GMBCG J141.68858+29.56935	0.29165 ... 0.4935 0.476 0.191
67	15:03:01.311	+27:57:48.781	WHL J150303.7+275519	0.5292
69	14:33:54.319	+50:40:45.173	ZwCl 1432.0+5054 GMBCG J218.43091+50.67096	0 0.38
70	08:53:00.399	+26:22:13.805	GMBCG J133.25279+26.36150 WHL J085254.0+262117	0.452 0.4549
72	11:00:10.270	+19:16:17.104	WHL J110014.2+191622 WHL J110003.2+191656	0.2382 0.4442
74	13:26:36.060	+53:53:57.959	WHL J132627.0+535348 GMBCG J201.72979+53.87878	0.375 0.327
75	01:19:34.439	+14:52:08.957	Abell 175 WHL J011938.3+145352 MaxBCG J019.90953+14.89798	0.1292 0.1289 0.14315
77	11:56:12.252	-00:21:02.814	SDSS CE J179.044357-00.342619 GMBCG J179.08749-00.37107	0.26537 0.199
79	12:12:08.759	+27:34:06.919	NSCS J121218+273325 WHL J121218.5+273255 GMBCG J182.99449+27.54719	0 0.3464 0.447
80	16:16:27.616	+58:12:38.798	WHL J161644.8+581118	0.2724
81	12:58:32.002	+43:59:47.314	WHL J125835.3+440102	0.5064
82	08:07:56.920	+65:25:07.350	NSC J080809+652543	0.1263
83	10:50:20.408	+28:28:04.966	GMBCG J162.56190+28.50020 WHL J105022.4+282439	0.411 0.4712
84	23:19:33.487	-01:19:26.377	NSCS J231933-011656 ZwCl 2316.8-0135	0.3 ...
85	09:21:11.999	+30:29:24.946	SHELS J0921.2+3028 [AWM2009] Cluster 1C	0.427 0.427
87	12:06:57.409	+30:29:22.828	NSCS J120702+303056 WHL J120654.8+303119 WHL J120708.2+302741	0.21 0.4916 0.4629
88	15:48:35.149	+17:02:22.535	WHL J154840.1+170448	0.3998
89	09:11:06.757	+61:08:18.085	NSC J091110+610734 Abell 747 GMBCG J137.72824+61.09600	0.2959 ... 0.322
91	08:22:49.875	+41:28:12.007	WHL J082247.8+412744 GMBCG J125.67646+41.45847	0.4664 0.47
92	23:03:44.474	+00:09:38.406	GMBCG J345.89121+00.14293 GMBCG J139.05662-00.42820 GMBCG J139.03846-00.40449	0.525 0.217 0.345
93	09:16:14.956	-00:25:31.237	Abell 776 WHL J091605.7-002324 GMBCG J139.11397-00.43552	0.33594 0.3208 0.433
94	12:01:25.380	+23:50:58.316	WHL J120122.5+235110 NSC J120127+235149 MaxBCG J180.32322+23.84515 GMBCG J180.35485+23.89116	0.26735 0.2471 0.22955 0.363

TABLE 3
CONTINUED.

Rank	RA	Dec	Cluster ^a	Redshift ^b
96	12:42:19.077	+40:23:40.425	WHL J124235.9+402255	0.4024
			WHL J124201.4+402335	0.4462
97	11:59:04.900	+51:11:15.803	WHL J115921.9+511238	0.388
98	11:11:23.230	+26:01:58.357	WHL J111123.2+260158	0.3325
			GMBCG J167.84231+26.02512	0.324
			GMBCG J167.85188+26.01246	0.177
99	11:23:08.271	+54:01:58.928	WHL J112247.2+540052	0.5005
100	14:32:40.352	+31:41:36.116	GMBCG J218.15811+31.64695	0.158
			MaxBCG J218.15809+31.64695	0.132
101	12:45:04.700	+02:29:08.618	GMBCG J191.25782+02.50588	0.33
			WHL J124501.2+023155	0.4881
103	09:15:50.686	+42:57:08.567	WHL J091550.7+425708	0.5303
			GMBCG J138.91793+42.95508	0.415
104	13:41:08.628	+12:33:45.316	WHL J134111.8+123303	0.5622
105	12:25:49.069	+08:24:48.700	WHL J122555.2+082243	0.4821
106	08:31:34.886	+26:52:25.307	WHL J083137.5+265054	0.4869
			GMBCG J127.93257+26.89906	0.26735
			GMBCG J127.85854+26.83155	0.453
107	10:14:11.602	+22:31:53.131	GMBCG J153.54834+22.53144	0.484
			WHL J101407.7+223015	0.4663
			GMBCG J153.54087+22.49259	0.516
108	15:36:44.604	+02:46:50.702	WHL J153646.4+024614	0.5121
			GMBCG J234.20097+02.75082	0.209
109	14:54:16.517	+04:34:40.491	WHL J145416.5+043440	0.3354
110	15:27:45.828	+06:52:33.629	SDSS J1527+0652 CLUSTER	0.4
			WHL J152745.8+065233	0.3812
			SDSS J1527+0652	0.39
111	00:06:11.544	-10:28:19.512	WHL J000611.5-102819	0.23495
			WHL J000614.3-102820	0.5158
			GMBCG J001.53135-10.50724	0.221
			GMBCG J001.53243-10.42147	0.175
114	00:15:23.386	-09:18:51.103	WHL J001513.3-091806	0.35
			WHL J001526.4-092207	0.4883
115	11:16:01.248	+18:24:23.300	WHL J111601.2+182423	0.4605
118	10:42:47.206	+33:12:17.845	WHL J104253.7+331254	0.5057
119	15:33:49.313	+02:38:36.105	WHL J153342.2+023744	0.5101
			WHL J153354.5+024135	0.5622
120	17:52:27.692	+60:10:12.774	WHL J175236.4+601045	0.4602
121	12:08:19.794	+61:22:03.732	WHL J120825.8+612054	0.5178
122	01:19:07.658	-09:34:02.693	GMBCG J019.79456-09.57832	0.348
			WHL J011916.4-093421	0.3505
123	09:38:11.613	+27:35:43.705	GMBCG J144.56963+27.58991	0.334
			WHL J093807.1+273749	0.4954
			GMBCG J144.49716+27.62634	0.422
125	14:52:00.837	+01:06:56.447	SDSS CE J223.007248+01.113963	0.37883
			WHL J145211.5+010748	0.3927
			SDSS CE J223.038879+01.152872	0.41286
			GMBCG J223.04780+01.15035	0.392
126	12:24:45.458	-00:39:14.796	NSCS J122447-004029	0.47
			WHL J122447.3-004056	0.4777
			GMBCG J186.15220-00.62346	0.403
127	15:54:59.348	+51:37:23.214	WHL J155447.4+513757	0.48
			GMBCG J238.70078+51.64642	0.467
129	12:19:21.841	+50:53:28.236	WHL J121917.6+505432	0.5327
			GMBCG J184.80005+50.93515	0.471
			GMBCG J184.75315+50.88179	0.372
130	09:51:40.088	-00:14:20.218	GMBCG J147.91704-00.23895	0.417
			SDSS CE J147.900848-00.253642	0.39017
			WHL J095148.5-001419	0.4168
131	00:51:24.585	-10:49:09.758	WHL J005121.4-104941	0.4847
132	22:26:27.277	+00:53:29.136	WHL J222624.0+005405	0.2771
134	15:50:36.108	+39:48:56.718	WHL J155036.6+394941	0.5004
			GMBCG J237.64892+39.78190	0.464
			NSCS J155027+394752	0.37

TABLE 3
CONTINUED.

Rank	RA	Dec	Cluster ^a	Redshift ^b
135	11:33:41.604	+39:52:25.291	GMBCG J173.39894+39.87612	0.437
			GMBCG J173.46103+39.87940	0.282
			Abell 1310	0.2619
			NSCS J113327+395228	0.47
			WHL J113353.5+395019	0.2755
136	13:01:02.878	+05:35:29.711	WHL J130106.9+053411	0.4817
			NSCS J130107+053314	0.25
138	11:33:37.447	+66:24:44.842	Abell 1302	0.1165
			WHL J113314.7+662246	0.12155
139	01:57:54.644	-00:57:11.347	SDSS CE J029.529423-00.979300	0.39017
140	11:13:46.352	+56:40:34.462	WHL J111344.3+564102	0.4754
			GMBCG J168.43311+56.64864	0.513
			GMBCG J168.44920+56.72458	0.474
141	14:44:19.496	+16:20:12.303	WHL J144428.9+162016	0.3955
			GMBCG J221.04927+16.35866	0.362
			GMBCG J221.08712+16.29277	0.338
144	10:27:02.072	+09:16:40.107	WHL J102702.1+091640	0.5496
145	16:48:00.199	+33:40:03.887	WHL J164803.8+334149	0.29975
			WHL J164745.7+334127	0.5307
146	10:22:32.057	+50:07:07.870	Abell 980	0.1582
			[EAD2007] 047	0.15718
147	09:26:51.422	+04:58:17.559	GMBCG J141.70184+04.96670	0.401
			NSC J092656+045928	0.2845
			ZwCl 0924.4+0511	0.2701
			GMBCG J141.69697+05.00110	0.486
			GMBCG J141.69759+05.02156	0.455
148	12:17:31.158	+36:41:11.240	GMBCG J141.76983+04.97938	0.25385
			WHL J121731.9+364112	0.3916
			SDSS J1217+3641 CLUSTER	0.364
149	11:53:05.648	+41:45:20.510	GMBCG J184.44333+36.68439	0.354
			NSCS J115309+414558	0.3
150	14:33:05.416	+51:03:16.905	WHL J115312.2+414444	0.29165
151	09:01:04.594	+39:54:49.063	WHL J143254.9+510154	0.4819
152	10:50:38.567	+35:49:12.425	GMBCG J135.26913+39.91365	0.541
154	08:50:07.915	+36:04:13.650	WHL J105038.6+354912	0.5021
			ZwCl 0847.2+3617	0.378
			GMBCG J132.49437+36.10756	0.284
156	08:45:43.999	+30:10:07.090	GMBCG J132.52774+36.01979	0.241
			WHL J084544.0+301007	0.4959
			GMBCG J131.39803+30.18358	0.428
			NSC J084530+300943	0.1253
157	14:55:07.993	+38:36:04.879	WHL J084530.0+300839	0.4025
			GMBCG J223.76805+38.61049	0.23
			ZwCl 1453.3+3849	...
			NSC J145457+383607	0.326
159	11:07:19.334	+53:04:17.938	WHL J145452.1+383716	0.3847
			GMBCG J166.86887+53.04094	0.462
			WHL J110708.1+530129	0.4296
160	15:38:02.025	+39:27:39.159	SDSS J1537+3926 CLUSTER	0.444
			NSCS J153814+392905	0.23
			NSC J153747+392702	0.2532
			WHL J153754.2+392444	0.409
161	01:03:24.248	+00:55:37.011	SDSS CE J015.847747+00.930720	0.2994
			SDSS CE J015.862271+00.873928	0.37883
162	10:40:17.611	+54:37:08.607	WHL J104016.0+543753	0.47
			GMBCG J160.02689+54.62449	0.391
			GMBCG J160.01506+54.57856	0.478
163	12:28:58.786	+53:37:27.671	WHL J122906.7+533551	0.5012
164	15:38:04.005	+39:22:32.253	WHL J153754.2+392444	0.409
166	09:50:00.059	+17:04:27.060	GMBCG J147.48329+17.07628	0.283
			GMBCG J147.50544+17.11794	0.443
			GMBCG J147.46139+17.04589	0.354
			WHL J094951.3+170701	0.3638

TABLE 3
CONTINUED.

Rank	RA	Dec	Cluster ^a	Redshift ^b
168	12:34:49.804	+23:03:42.109	WHL J123446.3+230217 NSC J123444+230059 ZwCl 1232.1+2319	0.3238 0.4125 ...
169	01:27:10.589	+23:14:19.797	Abell 196	...
170	13:15:23.033	-02:50:35.192	WHL J131515.4-024840	0.4112
171	11:39:02.869	+47:04:43.290	GMBCG J174.78774+47.10125 GMBCG J174.81035+47.03759	0.323 0.44
172	14:31:48.010	+09:00:15.869	NSCS J143159+090154	0.38
173	09:47:14.189	+38:10:22.088	WHL J094714.2+381022 GMBCG J146.78369+38.19401 GMBCG J146.85598+38.14762	0.4353 0.328 0.442
174	12:17:05.124	+26:05:18.445	WHL J121705.1+260518	0.476
175	13:26:25.383	+53:24:58.472	GMBCG J201.55655+53.44045	0.504
176	01:53:42.190	+05:35:44.062	NSCS J015338+053638	0.29
177	10:54:40.435	+55:23:56.307	GMBCG J163.66850+55.39898 WHL J105444.1+552059	0.487 0.4893
182	14:37:17.666	+34:18:22.187	NSC J143709+341851 GMBCG J219.34342+34.33407 WHL J143731.1+341834 WHL J143713.7+341530 GMBCG J219.31933+34.25157	0.2862 0.393 0.3808 0.5426 0.541
183	14:15:08.392	-00:29:35.680	WHL J141508.4-002935 SDSS CE J213.781525-00.487651 [DDM2004] J141505.03-002908.1	0.1303 0.14056 0.141
184	20:53:55.128	-06:34:51.054	GMBCG J313.43167-06.55856	0.481
185	12:35:44.353	+35:32:47.968	WHL J123549.2+353445	0.4851
186	11:52:35.385	+37:15:43.111	WHL J115235.4+371543 NSC J115231+371553	0.1475 0.1175
187	14:45:34.036	+48:00:12.417	WHL J144534.0+480012 GMBCG J221.47262+47.98388	0.5145 0.422
188	08:40:08.745	+21:56:03.214	WHL J084005.8+215315	0.4454
189	13:48:53.073	+57:23:46.617	WHL J134850.1+572147 Abell 1805 GMBCG J207.24819+57.44672	0.28895 ... 0.312
190	13:07:03.631	+46:33:47.849	[EAD2007] 037 GMBCG J196.75262+46.56389 WHL J130657.3+463206 GMBCG J196.70832+46.55927 Abell 1682 GMBCG J196.70330+46.60084	0.24656 0.337 0.2081 0.245 0.2339 0.415
191	11:40:40.199	+44:07:40.291	MaxBCG J175.15921+44.11784 GMBCG J175.15828+44.14893 NSCS J114032+440607 WHL J114034.8+440541 ZwCl 1137.8+4425	0.14585 0.487 0.42 0.4529 ...
192	14:48:20.246	+20:43:31.168	WHL J144820.4+204437 GMBCG J222.10454+20.75123	0.5046 0.449
193	12:41:56.529	+03:43:59.760	GMBCG J190.52490+03.76859 WHL J124158.0+034721	0.357 0.3915
194	08:41:23.880	+25:13:05.204	WHL J084123.9+251305 GMBCG J130.35004+25.17696	0.4655 0.475
196	00:24:59.715	+08:26:16.778	NSCS J002458+082639	0.43
197	15:50:16.987	+34:18:33.901	WHL J155025.7+341708 WHL J155006.3+341917 GMBCG J237.60955+34.26717	0.4297 0.4329 0.468
198	01:37:18.176	+07:55:44.482	Abell 220	0.33
199	11:05:20.978	+17:37:16.830	GMBCG J166.33740+17.62134 GMBCG J166.30451+17.61325 WHL J110521.7+173505	0.497 0.375 0.5099
200	03:33:12.198	-06:52:24.614	WHL J033303.7-065233	0.2918

REFERENCES

- Abate, A., Wittman, D., Margoniner, V. E., Bridle, S. L., Gee, P., Tyson, J. A., & Dell'Antonio, I. P. 2009, *ApJ*, 702, 603
- Abell, G. O., Corwin, Jr., H. G., & Olowin, R. P. 1989, *ApJS*, 70, 1
- Ahn, C. P., et al. 2012, *ApJS*, 203, 21
- Angulo, R. E., Springel, V., White, S. D. M., Jenkins, A., Baugh, C. M., & Frenk, C. S. 2012, *MNRAS*, 426, 2046
- Auger, M. W., Treu, T., Gavazzi, R., Bolton, A. S., Koopmans, L. V. E., & Marshall, P. J. 2010, *ApJ*, 721, L163
- Bartelmann, M., Huss, A., Colberg, J. M., Jenkins, A., & Pearce, F. R. 1998, *A&A*, 330, 1
- Bartelmann, M., Steinmetz, M., & Weiss, A. 1995, *A&A*, 297, 1
- Behroozi, P. S., Conroy, C., & Wechsler, R. H. 2010, *ApJ*, 717, 379
- Behroozi, P. S., Wechsler, R. H., & Conroy, C. 2012, *ApJ*, submitted (arXiv:1207.6105)
- Bell, E. F., & de Jong, R. S. 2001, *ApJ*, 550, 212
- Bernardi, M., et al. 2003, *AJ*, 125, 1849
- Böhringer, H., et al. 2000, *ApJS*, 129, 435
- Bonamente, M., Joy, M., LaRoque, S. J., Carlstrom, J. E., Nagai, D., & Marrone, D. P. 2008, *ApJ*, 675, 106
- Bouwens, R., et al. 2012, *ApJ*, submitted (arXiv:1211.2230)
- Bradač, M., et al. 2012, *ApJ*, 755, L7
- Bradley, L. D., et al. 2008, *ApJ*, 678, 647
- . 2012, *ApJ*, 747, 3
- Brammer, G. B., et al. 2012, *ApJ*, 758, L17
- Bruzual, G., & Charlot, S. 2003, *MNRAS*, 344, 1000
- Cacciato, M., van den Bosch, F. C., More, S., Li, R., Mo, H. J., & Yang, X. 2009, *MNRAS*, 394, 929
- Cacciato, M., van den Bosch, F. C., More, S., Mo, H., & Yang, X. 2013a, *MNRAS*, 430, 767
- Cacciato, M., van Uitert, E., & Hoekstra, H. 2013b, *MNRAS*, submitted (arXiv:1207.6105)
- Cappellari, M., et al. 2012, *Nature*, 484, 485
- Coe, D., et al. 2012, *ApJ*, 757, 22
- . 2013, *ApJ*, 762, 32
- Conroy, C., & van Dokkum, P. G. 2012, *ApJ*, 760, 71
- Conroy, C., & Wechsler, R. H. 2009, *ApJ*, 696, 620
- Cool, R. J., et al. 2008, *ApJ*, 682, 919
- Coziol, R., Andernach, H., Caretta, C. A., Alamo-Martínez, K. A., & Tago, E. 2009, *AJ*, 137, 4795
- Csabai, I., et al. 2003, *AJ*, 125, 580
- Dawson, K. S., et al. 2013, *AJ*, 145, 10
- de Jong, J. T. A., Verdoes Kleijn, G. A., Kuijken, K. H., & Valentijn, E. A. 2013, *Experimental Astronomy*, 35, 25
- De Lucia, G., Springel, V., White, S. D. M., Croton, D., & Kauffmann, G. 2006, *MNRAS*, 366, 499
- Desai, V., Dalcanton, J. J., Mayer, L., Reed, D., Quinn, T., & Governato, F. 2004, *MNRAS*, 351, 265
- Ebeling, H., Edge, A. C., & Henry, J. P. 2001, *ApJ*, 553, 668
- Eisenstein, D. J., et al. 2001, *AJ*, 122, 2267
- . 2003, *ApJ*, 585, 694
- . 2005, *ApJ*, 633, 560
- Estrada, J., et al. 2007, *ApJ*, 660, 1176
- Ford, J., et al. 2012, *ApJ*, 754, 143
- Frye, B. L., et al. 2012, *ApJ*, 754, 17
- Gal, R. R., de Carvalho, R. R., Lopes, P. A. A., Djorgovski, S. G., Brunner, R. J., Mahabal, A., & Odewahn, S. C. 2003, *AJ*, 125, 2064
- Geller, M. J., Dell'Antonio, I. P., Kurtz, M. J., Ramella, M., Fabricant, D. G., Caldwell, N., Tyson, J. A., & Wittman, D. 2005, *ApJ*, 635, L125
- Gladders, M. D., Hoekstra, H., Yee, H. K. C., Hall, P. B., & Barrientos, L. F. 2003, *ApJ*, 593, 48
- Gladders, M. D., & Yee, H. K. C. 2000, *AJ*, 120, 2148
- Gonzalez, A. H., Zaritsky, D., & Zabludoff, A. I. 2007, *ApJ*, 666, 147
- Gonzalez, A. H., et al. 2012, *ApJ*, 753, 163
- Goto, T., et al. 2002, *AJ*, 123, 1807
- Hall, N., et al. 2012, *ApJ*, 745, 155
- Hao, J., et al. 2009, *ApJ*, 702, 745
- . 2010, *ApJS*, 191, 254
- Hennawi, J. F., Dalal, N., Bode, P., & Ostriker, J. P. 2007, *ApJ*, 654, 714
- Hennawi, J. F., et al. 2008, *AJ*, 135, 664
- Hikage, C., Mandelbaum, R., Takada, M., & Spergel, D. N. 2012, arXiv:1211.1009
- Hildebrandt, H., et al. 2011, *ApJ*, 733, L30
- Ho, S., Lin, Y.-T., Spergel, D., & Hirata, C. M. 2009, *ApJ*, 697, 1358
- Hoekstra, H., Hartlap, J., Hilbert, S., & van Uitert, E. 2011, *MNRAS*, 412, 2095
- Huang, X., et al. 2009, *ApJ*, 707, L12
- Kaiser, N. 2004, in *Society of Photo-Optical Instrumentation Engineers (SPIE) Conference Series*, Vol. 5489, Society of Photo-Optical Instrumentation Engineers (SPIE) Conference Series, ed. J. M. Oschmann, Jr., 11–22
- Kauffmann, G., et al. 2003, *MNRAS*, 341, 33
- Kneib, J., Ellis, R. S., Santos, M. R., & Richard, J. 2004, *ApJ*, 607, 697
- Koester, B. P., et al. 2007, *ApJ*, 660, 239
- Laporte, N., et al. 2011, *A&A*, 531, A74+
- Laureijs, R., et al. 2011, arXiv:1110.3193
- Leauthaud, A., et al. 2012, *ApJ*, 744, 159
- Li, C., Kauffmann, G., Jing, Y. P., White, S. D. M., Börner, G., & Cheng, F. Z. 2006, *MNRAS*, 368, 21
- Lidman, C., et al. 2012, *MNRAS*, 427, 550
- Lin, Y.-T., & Mohr, J. J. 2004, *ApJ*, 617, 879
- Lin, Y.-T., Mohr, J. J., Gonzalez, A. H., & Stanford, S. A. 2006, *ApJ*, 650, L99
- Lin, Y.-T., Mohr, J. J., & Stanford, S. A. 2003, *ApJ*, 591, 749
- . 2004, *ApJ*, 610, 745
- Livermore, R. C., et al. 2012, *MNRAS*, 427, 688
- Lopes, P. A. A., de Carvalho, R. R., Gal, R. R., Djorgovski, S. G., Odewahn, S. C., Mahabal, A. A., & Brunner, R. J. 2004, *AJ*, 128, 1017
- Mandelbaum, R., Seljak, U., Kauffmann, G., Hirata, C. M., & Brinkmann, J. 2006, *MNRAS*, 368, 715
- Mantz, A., Allen, S. W., Ebeling, H., Rapetti, D., & Drlica-Wagner, A. 2010, *MNRAS*, 406, 1773
- Marriage, T. A., et al. 2011, *ApJ*, 737, 61
- Meneghetti, M., Bartelmann, M., & Moscardini, L. 2003, *MNRAS*, 340, 105
- More, S. 2012, *ApJ*, 761, 127
- More, S., van den Bosch, F. C., Cacciato, M., Mo, H. J., Yang, X., & Li, R. 2009, *MNRAS*, 392, 801
- Moster, B. P., Somerville, R. S., Maubetsch, C., van den Bosch, F. C., Macciò, A. V., Naab, T., & Oser, L. 2010, *ApJ*, 710, 903
- Oke, J. B., & Gunn, J. E. 1983, *ApJ*, 266, 713
- Padmanabhan, N., et al. 2005, *MNRAS*, 359, 237
- . 2007, *MNRAS*, 378, 852
- Pelló, R., Schaerer, D., Richard, J., Le Borgne, J., & Kneib, J. 2004, *A&A*, 416, L35
- Pérez-González, P. G., et al. 2008, *ApJ*, 675, 234
- Popesso, P., Böhringer, H., Romaniello, M., & Voges, W. 2005, *A&A*, 433, 415
- Postman, M., et al. 2012, *ApJS*, 199, 25
- Reid, B. A., & Spergel, D. N. 2009, *ApJ*, 698, 143
- Richard, J., Pelló, R., Schaerer, D., Le Borgne, J., & Kneib, J. 2006, *A&A*, 456, 861
- Richard, J., Stark, D. P., Ellis, R. S., George, M. R., Egami, E., Kneib, J., & Smith, G. P. 2008, *ApJ*, 685, 705
- Ross, A. J., et al. 2011, *MNRAS*, 417, 1350
- Salpeter, E. E. 1955, *ApJ*, 121, 161
- Schaerer, D., & Pelló, R. 2005, *MNRAS*, 362, 1054
- Sharon, K., Gladders, M. D., Rigby, J. R., Wuyts, E., Koester, B. P., Bayliss, M. B., & Barrientos, L. F. 2012, *ApJ*, 746, 161
- Skibba, R. A., van den Bosch, F. C., Yang, X., More, S., Mo, H., & Fontanot, F. 2011, *MNRAS*, 410, 417
- Spiniello, C., Trager, S. C., Koopmans, L. V. E., & Chen, Y. P. 2012, *ApJ*, 753, L32
- Springel, V., et al. 2005, *Nature*, 435, 629
- Stark, D. P., Ellis, R. S., Richard, J., Kneib, J.-P., Smith, G. P., & Santos, M. R. 2007, *ApJ*, 663, 10
- Sunyaev, R. A., & Zeldovich, Y. B. 1972, *Comments on Astrophysics and Space Physics*, 4, 173
- Tinker, J., Kravtsov, A. V., Klypin, A., Abazajian, K., Warren, M., Yepes, G., Gottlöber, S., & Holz, D. E. 2008, *ApJ*, 688, 709
- Tinker, J. L., Weinberg, D. H., Zheng, Z., & Zehavi, I. 2005, *ApJ*, 631, 41
- Treu, T., Auger, M. W., Koopmans, L. V. E., Gavazzi, R., Marshall, P. J., & Bolton, A. S. 2010, *ApJ*, 709, 1195
- Treu, T., Ellis, R. S., Liao, T. X., & van Dokkum, P. G. 2005a, *ApJ*, 622, L5
- Treu, T., et al. 2005b, *ApJ*, 633, 174
- Ueda, Y., Ishisaki, Y., Takahashi, T., Makishima, K., & Ohashi, T. 2001, *ApJS*, 133, 1
- van Dokkum, P. G., & Conroy, C. 2012, *ApJ*, 760, 70
- van Dokkum, P. G., & Stanford, S. A. 2003, *ApJ*, 585, 78
- Van Waerbeke, L., Hildebrandt, H., Ford, J., & Milkeraitis, M. 2010, *ApJ*, 723, L13
- Vanderlinde, K., et al. 2010, *ApJ*, 722, 1180
- Vikhlinin, A., et al. 2009, *ApJ*, 692, 1033
- von der Linden, A., Best, P. N., Kauffmann, G., & White, S. D. M. 2007, *MNRAS*, 379, 867
- Wen, Z. L., Han, J. L., & Liu, F. S. 2009, *ApJS*, 183, 197
- . 2012, *ApJS*, 199, 34
- White, M., et al. 2011, *ApJ*, 728, 126

- Williamson, R., et al. 2011, *ApJ*, 738, 139
- Wong, K. C., Ammons, S. M., Keeton, C. R., & Zabludoff, A. I. 2012, *ApJ*, 752, 104
- Yang, X., Mo, H. J., & van den Bosch, F. C. 2008, *ApJ*, 676, 248
- Yuan, T.-T., Kewley, L. J., Swinbank, A. M., & Richard, J. 2012, *ApJ*, 759, 66
- Zaritsky, D., Gonzalez, A. H., & Zabludoff, A. I. 2006, *ApJ*, 638, 725
- Zehavi, I., et al. 2005, *ApJ*, 621, 22
- Zheng, W., et al. 2009, *ApJ*, 697, 1907
- . 2012, *Nature*, 489, 406
- Zitrin, A., Broadhurst, T., Bartelmann, M., Rephaeli, Y., Oguri, M., Benítez, N., Hao, J., & Umetsu, K. 2012, *MNRAS*, 423, 2308
- Zitrin, A., et al. 2011, *ApJ*, 742, 117
- Zwicky, F., Herzog, E., Wild, P., Karpowicz, M., & Kowal, C. T. 1961, *Catalogue of galaxies and of clusters of galaxies*, Vol. I